A Search for Excited Fermions in Electron-Proton Collisions at HERA

ZEUS Collaboration
(September 28, 1994)

Abstract

A search for excited states of the standard model fermions was performed using the ZEUS detector at the HERA electron-proton collider, operating at a centre of mass energy of 296 GeV. In a sample corresponding to an integrated luminosity of 0.55 pb^{-1}, no evidence was found for any resonant state decaying into final states composed of a fermion and a gauge boson. Limits on the coupling strength times branching ratio of excited fermions are presented for masses between 50 GeV and 250 GeV, extending previous search regions significantly.

I. INTRODUCTION

An intriguing puzzle in high energy physics is the regular pattern presented by the three fermion families. In the history of physics similar phenomena have been explained by a new level of substructure. So far, there has been no experimental support for any theory of new constituents and their interactions. The main difficulty is to reconcile the mass scale of presently known particles with a much larger scale of compositeness, Λ. The absence of any evidence of compositeness in current experimental data suggests that Λ is at least 1 TeV.

One potential effect of lepton and/or quark substructure would be the existence of excited fermion states e^*, ν^*, and q^* [1] [2]. In phenomenological models [3] [4] it is assumed that any theory of compositeness at large mass scales must have a low energy limit that preserves the symmetries of the standard model, therefore the excited fermions postulated in these "effective Lagrangian" theories should form weak iso-doublets and carry electroweak charges similar to those of the ordinary fermions. At HERA, possible magnetic-transition couplings of the electron (quark) to the first generation heavy fermions would allow single production of e^* (q^*) through t-channel γ and Z boson exchange and of ν^* (q^*) through t-channel W boson exchange. An example is shown in Figure 1.

We report on a search for any state which decays into a gauge boson and a fundamental fermion in the reaction $ep \rightarrow f^*X$, with an integrated luminosity of 0.55 pb^{-1}, a 20-fold increase in statistics in comparison with previous HERA results [5] [6]. In addition, it presents the results of the first search for q^* production through electroweak coupling.

This paper is structured in the following manner: the next section describes the detector. Section III defines the kinematic variables relevant to this analysis. The event topologies expected for excited fermion events and the selection of data consistent with these topologies are discussed in Section IV. Section V discusses models (see the appendix for details) which we used to develop our selection procedures and later used to interpret our results. The event selection procedure is explained in Section VI. Experimental results for the e^*, ν^*, and q^* searches are then presented in Sections VII and VIII. The theoretical implications of these results and limits on the excited fermion coupling strengths are discussed in Sections IX and X.

II. DETECTOR AND RUNNING CONDITIONS

The data used in this analysis were taken in 1993 with the ZEUS detector at the electron proton collider HERA. During this period, HERA was operated with 26.7 GeV electrons and 820 GeV protons, corresponding to a center of mass energy ($\sqrt{s}$) of 296 GeV. Of the 220 buckets, the machine was filled with 84 pairs of electron and proton bunches colliding every 96 ns. There were also 6 additional proton and 10 additional electron bunches left unpaired to allow studies of beam related backgrounds. In addition, we triggered on 28 empty bunches, which were used in this analysis to estimate the cosmic-ray background.

The average interaction point was located [1] at $z = -6.1$ cm with a spread of $\sigma_z = 10.4$ cm. The dominant contribution to the spread of the interaction vertex was the length of the proton bunch.

The ZEUS detector is described in detail elsewhere [7] [8]. This analysis relies mainly on the high-resolution depleted-uranium scintillator calorimeter and the central tracking detectors. A beam monitor and a wall of scintillator outside the main detector are used to tag interactions of the proton beam upstream of the detector. The calorimeter covers 99.7% of the solid angle. It consists of three parts covering different regions of the polar angle θ: forward (FCAL, $2.6^0 < \theta < 36.7^0$), barrel (BCAL, $36.7^0 < \theta < 129.1^0$), and rear (RCAL, $129.1^0 < \theta < 176.2^0$). Each part is subdivided into towers of typically 20×20 cm^2 transverse dimension, which in turn are segmented in depth into electromagnetic and hadronic sections. To improve spatial resolution, the electromagnetic sections are subdivided transversely into cells of 5×20 cm^2 (10×20 cm^2 for the rear calorimeter). Each cell is read out by two photomultiplier tubes, providing redundancy and a position measurement within the cell. Under test beam conditions [9], the calorimeter has an energy resolution of $\sigma_E/E = 18\%/\sqrt{E(GeV)}$ for electrons and $\sigma_E/E = 35\%/\sqrt{E(GeV)}$ for hadrons. In addition, the calorimeter provides a time resolution better than 1 ns for energy deposits greater than 4.5 GeV, which is used in background rejection. The calorimeter noise, dominated by the uranium radioactivity, is in the range 15-19 MeV for electromagnetic cells and 24-30 MeV for hadronic cells. Integrated over time (20ms), this uranium radioactivity is used to monitor the signal gain of each calorimeter channel. To minimize the effect of the noise on the event reconstruction, in order for a cell to be used in this analysis, we required a minimum energy deposit of 60 (110) MeV in an electromagnetic (hadronic) cell.

Charged particle detection is performed by two concentric cylindrical drift chambers, the vertex detector and the central tracking detector occupying the space between the beam pipe and the superconducting coil of the magnet. In 1993, the detector was operated with a magnetic field of 1.43 T. The precision vertex detector is surrounded by the main drift chamber, which consists of 72 cylindrical drift chamber layers organized into 9 superlayers. [8]

The luminosity is determined by measuring the rate of energetic bremsstrahlung photons produced in the process $ep \rightarrow ep\gamma$. The photons are detected in a lead-scintillator calorimeter placed at $z = -107$ m. The background rate from collisions with the residual gas in the beam pipe was subtracted using the unpaired electron bunches. The integrated luminosity used in this analysis corresponds to 0.55 pb^{-1} with an estimated systematic error of 3.3%.

III. KINEMATICS

The selection of candidate events for excited fermion decays started with the data acquisition trigger, followed by the offline event reconstruction and the final analysis. To

---

[1] ZEUS used a right-handed coordinate system, centered at the nominal interaction point, defined with positive z along the direction of the proton beam and positive y upwards.

demonstrate the motivation behind the selection criteria, we first discuss the kinematics of the events expected from excited fermion states, in the reaction:

$$ep \rightarrow f^* X$$

with the f^* decaying in the detector. The kinematic quantities relevant to this analysis are presented in this section. In the interaction of the incident electron (with beam energy E_e and four-momentum k) and incident proton (with beam energy E_p and four-momentum P), the square of the four-momentum transfer, carried by the propagator, is denoted by $-Q^2$. In the case of neutral current (NC) deep inelastic scattering (DIS) or excited quark (q^*) production, this is defined as:

$$-Q_l^2 \equiv q^2 \equiv (k' - k)^2$$

where k' is the four-momentum of the scattered electron and the quantity q^2 is the Mandelstam variable t. By comparison, for excited lepton (l^*) production, this is defined as:

$$-Q_{l*}^2 \equiv (k^{*\prime} - k)^2$$

where $k^{*\prime}$ is the four-momentum of the excited lepton, respectively (see Figure 1). Note that for excited leptons, in those modes in which an electron is expected to result from l^* decay, $-Q^2$ cannot be computed from the electron as it would be in an NC DIS interaction. In the naive quark-parton model, the momentum fraction, x, carried by the parton which couples to the exchanged particle, is defined by:

$$x \equiv -q^2 / P \cdot q.$$

The final state which results from the interaction may or may not contain an electron or other electromagnetic shower in the main ZEUS calorimeter. When the final state does have an electromagnetic shower, the polar angle and the energy of the shower are denoted by θ_{EM} and E_{EM} respectively. In channels where more than one electromagnetic shower is expected in the final state, the angles and energies are denoted by numbered subscripts after "EM" (e.g. $\theta_{EM\,2}$, $E_{EM\,2}$). The vector sum of transverse energy in calorimeter cells is referred to as p_T and its absolute value is called $\mathrm{p}_{T\ miss}$. Also used is $\mathrm{p}_{T\ miss}^{inner\ ring}$ which is the absolute value of the vector sum of transverse energy attributed only to the ring of FCAL cells nearest the beampipe. The scalar sum of transverse energy is denoted by E_T. We define the quantities $E_T^{hadronic}$ and E_T^c which respectively denote the E_T associated only with the hadronic state excluding the ring of FCAL cells adjacent to the beampipe and the Monte Carlo generator-level E_T calculated excluding cones which approximate the beampipe. $M_{hadronic}$ is the effective mass measured by the calorimeter excluding the ring of FCAL cells adjacent to the beampipe and the electromagnetic shower associated with an f^* candidate decay. We define the quantity:

$$\delta \equiv \sum E_i (1 - cos\theta_i)$$

which, in events where visible energy is lost down the forward beampipe only, should be approximately equal to twice the incident electron beam energy due to energy conservation. The sum runs over all calorimeter cells with energies above the previously mentioned thresholds and the θ_i are calculated with respect to the measured interaction vertex.

IV. EXCITED FERMION TOPOLOGIES

In this analysis, excited fermions were searched for via their decays into a standard model fermion and a gauge boson. The final states considered are listed in Table I. Decays of excited fermions produce characteristic event topologies which allows one to distinguish them from neutral and charged current deep inelastic scattering (NC and CC DIS respectively) events as well as from photoproduction events. Due to their large mass, excited fermions would produce events with large transverse energy, E_T. The signature of decay modes involving neutrinos is missing transverse momentum, $\mathrm{p}_{T\ miss}$. For high-mass f^* decays with an e or γ in the final state, the electromagnetic shower tends to be boosted into the forward hemisphere, in contrast to low Q_l^2 NC DIS. Therefore we use the polar angle of the electromagnetic shower to distinguish between such f^* decays and NC DIS. Requiring that the electromagnetic shower energy exceeds a minimum value suppresses photoproduction background and reduces the number of fake candidates from $\pi^0 \to \gamma\gamma$ decays. It is worth noting that photoproduction is a significant background only in q^* decays. This is because the incident electron is often lost down the rear beampipe in both photoproduction and potential q^* production. Thus, a minimum cut on δ, which can be used to remove photoproduction in e^* modes, or a cut on $\mathrm{p}_{T\ miss}$, which can be used to remove photoproduction from ν^* modes, cannot be used in q^* modes.

TABLE I. Excited fermion decays and topologies, and backgrounds to f^* production. The event types listed as physics backgrounds (such as "Compton") refer to Standard Model processes which can have similar topologies and are discussed in Section IV The abbreviation "EM" stands for "electromagnetic."

Excited Fermion	Final State	Topology	Principal Background
$e^* \to e\gamma$	$e\gamma$	2 EM clusters	NC DIS, Compton
$e^* \to eZ$	$eq\bar{q}$	1 EM cluster, high E_T, jets	NC DIS
$e^* \to eZ$	$ee\bar{e}$	3 EM clusters, high E_T	NC DIS
$e^* \to eZ$	$e\nu\bar{\nu}$	1 EM cluster, missing p_T	CC DIS
$e^* \to \nu W$	$\nu q\bar{q}'$	high E_T, missing p_T, jets	CC DIS
$e^* \to \nu W$	$\nu e\bar{\nu}$	1 EM cluster, high E_T, missing p_T	NC+CC DIS
$\nu^* \to \nu\gamma$	$\nu\gamma$	1 EM cluster, missing p_T, jet(s)	NC DIS
$\nu^* \to \nu Z$	$\nu q\bar{q}$	high E_T, missing p_T, jets	CC DIS
$\nu^* \to \nu Z$	$\nu e\bar{e}$	2 EM clusters, missing p_T, jet(s)	CC DIS
$\nu^* \to eW$	$eq\bar{q}'$	1 EM cluster, high E_T, jets	NC DIS
$\nu^* \to eW$	$ee\bar{\nu}$	2 EM clusters, high E_T, missing p_T, jet(s)	NC+CC DIS
$q^* \to q\gamma$	$q\gamma$	1 EM cluster, high E_T, jet(s)	NC DIS, Photoproduction
$q^* \to qZ$	$qq\bar{q}'$	high E_T, jets	NC DIS, Photoproduction
$q^* \to qW$	$qq'\bar{q}''$	high E_T, jets	NC DIS, Photoproduction
$q^* \to qg$	qg	high E_T, jets	NC DIS, Photoproduction

V. MONTE CARLO SIMULATION

Monte Carlo event simulations were used to determine the detector acceptances and to correct for resolution effects. The detector simulation is based on GEANT [10] and incorporates our best knowledge of the experimental environment and trigger. Monte Carlo events are passed through the same analysis as the data.

A. Excited Fermion Production and Decay

A Monte Carlo simulation of excited fermion production and decay is required to develop efficient selection cuts and calculate acceptances. This analysis uses HEXF, [11] a generator for heavy excited fermion production, which is based on models by Hagiwara et al., Boudjema et al., and Baur et al. [3] [4]. Radiative corrections are included in this generator using the Weizsäcker-Williams approximation [12] and the MRSD_0 [13] set is used to model the parton density distributions inside the proton. The QCD cascade is modeled with LEPTO 6.1 [14] using first-order matrix elements and parton showers (MEPS). JETSET 7.3 [15] is used for the soft hadronization.

The HEXF generator models the production of excited fermions in ep scattering and their subsequent decay to standard fermions and gauge bosons. In this analysis, we considered the following f^* decay modes:

$$e^* \rightarrow e\gamma,\ eZ,\ \nu W$$

$$\nu^* \rightarrow \nu\gamma,\ \nu Z,\ eW$$

$$q^* \rightarrow q\gamma,\ qZ,\ qW,\ qg$$

where heavy bosons were subsequently allowed to decay according to their naturally occurring branching fractions [16].

B. Background Events

The DIS events with $Q_l^2 > 4\ \mathrm{GeV}^2$ were generated using the HERACLES [17] program, which includes first-order electroweak radiative corrections. The MRSD_0 [13] set was used for the parameterization of the parton density distributions. The hadronic final state was simulated using the colour dipole model [18] as implemented in ARIADNE 3.1 [19] for the QCD cascade, and JETSET 6.3 for the soft hadronization. To study the sensitivity of acceptance corrections to fragmentation models, a sample of DIS events was also generated using the LEPTO 6.1 [14] program which employs matrix elements and parton showers for the QCD cascades.

An additional background for elastic $e^* \rightarrow e\gamma$ decays, elastic Compton scattering, $ep \rightarrow e\gamma p$, was studied using the COMPTON 2.0 [20] generator. Inelastic Compton scattering (where the proton dissociates) is included in the HERACLES generator for DIS NC events.

Photoproduction at low Q_l^2 but with a large energy transfer from the photon to the hadronic final state can be a source of background to f^* production. We studied this effect by generating resolved and direct photoproduction events using the HERWIG [21] generator.

TABLE II. Background Monte Carlo samples. Generator level cuts on E_T^c are calculated excluding cones approximating the forward and rear beampipes.

Mode	Generator	PDF	Generator cuts	Luminosity pb^{-1}
NC-DIS	HERACLES	MRSD_0	$Q_l^2 > 4\ \mathrm{GeV}^2$	0.4
	+ ARIADNE		$Q_l^2 > 4\ \mathrm{GeV}^2$	
			$E_T^c > 14$ GeV	3.1
			$E(\theta > 155^0) < 7.5$ GeV	
	LEPTO, ME+PS	EHLQ1	$E_T > 30$ GeV	
			$\theta_e < 150^0$	3.2
CC-DIS	HERACLES	MRSD_0		
	+ ARIADNE			14.1
	LEPTO, ME+PS	EHLQ1		7.2
Compton	COMPTON 2.0		$E_{\gamma,e} >2$ GeV	
			$1^0 < \theta_{e,\gamma} < 179^0$	
			$E_\gamma + E_e >10$ GeV	0.5
$\gamma p \to X$ (direct)	HERWIG	MRSD_0	$E_T^c > 20$ GeV	1.7
$\gamma p \to X$ (direct)	HERWIG	MRSD_0	$E_T > 30$ GeV	2.2
$\gamma p \to X$ (resolved)	HERWIG	MRSD_0/GRV	$E_T^c > 20$ GeV	0.5
$\gamma p \to X$ (resolved)	HERWIG	MRSD_0/GRV	$E_T > 40$ GeV	2.0

Table II gives an overview of the Monte Carlo samples used in this analysis. For most Monte Carlo samples we have applied cuts at the generator level (see Table II) to reduce the total number of events that needed to be simulated. It should be noted (see Figure 2a) that generator-level E_T cuts in Table II have little effect on signal acceptances. Note also that we are interested in high-mass production, which requires large values of x ($x > 10^{-2}$), where differences between various parametrizations of the parton distribution functions (PDF's) are negligible.

VI. EVENT SELECTION

Data were collected with a three-stage trigger [22]: a deadtime-free pipeline first level trigger which was based on calorimeter energy thresholds, a second level trigger to reject obvious non-physics events, and a third level trigger which applied physics-based filters to select events for output to mass storage and offline analysis. Events surviving the third level trigger were passed through an offline reconstruction program, which employed an electromagnetic shower finding algorithm, an isolated muon finding algorithm, a jet finding algorithm, a vertex finding algorithm, and an energy clustering algorithm. Events passed this stage of analysis, hereafter called the preselection, if they fulfilled any one of the requirements:

- $(\delta > 25 \text{ GeV}) \quad \cdot \quad (N_{EM} > 0) \quad \cdot \quad (N_\mu < 1)$
- $(E_T > 20 \text{ GeV}) \quad \cdot \quad (\mathrm{p}_{T\ miss} > 8 \text{ GeV}) \quad \cdot \quad (N_\mu < 1)$
- $(E_T > 30 \text{ GeV}) \quad \cdot \quad (N_\mu < 1) \quad \cdot \quad (N_v > 0)$
- $(E_T - E_{T\ FCAL}^{cluster}[< 30\ cm] > 20 \text{ GeV}) \quad \cdot \quad (N_\mu < 1) \quad \cdot \quad (N_v > 0)$
- $(E_T > 8 \text{ GeV}) \quad \cdot \quad (N_\mu < 1) \quad \cdot \quad (N_v > 0) \quad \cdot \quad (\delta > 25 \text{ GeV})$
- $(\mathrm{p}_{T\ any\ jet} > 15 \text{ GeV}) \quad \cdot \quad (N_v > 0)$

where N_{EM} is the number of electromagnetic showers found, $N_v > 0$ means one or more vertices obtained from the reconstructed tracks, N_μ is the number of isolated muons, and $E_{T\ FCAL}^{cluster}[< 30 \text{ cm}]$ is the transverse energy from FCAL clusters centered within 30 cm of the beamline. All transverse energies excluded the inner ring of FCAL cells. Events with isolated muons were excluded from most categories to reduce cosmic-ray backgrounds. Approximately 250,000 events remained after the preselection.

After the offline reconstruction, we used refined timing information from the calorimeter and the reconstructed vertex position to reject background events by requiring that the vertex from calorimeter timing and the vertex from tracking be within 45 cm of one another. The cosmic-ray backgrounds were further suppressed by using timing differences between upper and lower regions of the calorimeter while beam-gas backgrounds were reduced by using timing differences between forward and rear regions of the calorimeter.

Events passing the following selection criteria (hereafter referred to as the "initial selection cuts") were used for the analysis:

- $\mathrm{p}_{T\ miss} > 8$ GeV
- $N_{EM} > 1, \theta_{EM} < 150^0$
- $(E_T > 30 \text{ GeV}) \quad \cdot \quad (\delta > 20 \text{ GeV})$
- -50 cm $< z_{\text{vertex}} <$ 40 cm.

Since the decay products of a massive resonance would be boosted strongly in the proton direction, limiting θ_{EM} retains high acceptance for excited fermion decays while substantially removing NC DIS and Compton events (Figure 2d). Unbalanced transverse momentum, $\mathrm{p}_{T\ miss}$, is the characteristic signature for events with neutrinos in the final state. As can be seen in Figure 2c, selecting events with $\mathrm{p}_{T\ miss} > 8$ GeV significantly reduced the NC DIS background. Photoproduction background was also significantly reduced by this cut. However, this cut did not suppress backgrounds from CC DIS events. Requiring $\delta > 20$ GeV reduced photoproduction backgrounds where the scattered electron remained in the beampipe.

Approximately 84,000 events passed these criteria (fiducial q^* cuts), and are hereafter referred to as the "fiducial q^* sample". Since we were principally interested in events with a possible heavy excited fermion decay, we required at least 30 GeV of transverse energy (E_T). Figure 2a shows transverse energy distributions obtained from signal and background Monte Carlo samples. Rejecting events with more than 5 GeV energy in a backward cone ($\theta > 150^0$) was a powerful tool in reducing the background from neutral current deep inelastic scattering (NC DIS) while maintaining high signal efficiency (Figure 2b) for excited lepton searches. Approximately 18,000 events remain after the application of the backward cone cut and the $E_T > 30$ GeV cut, hereafter referred to as the "fiducial l^* sample". The fiducial q^* cuts along with the two additional cuts mentioned above are referred to as the "fiducial l^* cuts". The backward cone cut was not applied in the search for excited quarks since a significant fraction of the electrons scattered at low Q_l^2 end up in the beampipe region of the RCAL.

The effects of the two (l^* and q^*) fiducial sample cuts on the acceptance of the various Monte Carlo samples (signal and background) can be found in Tables III, IV, and V.

TABLE III. Acceptances, in percent, for e^* and background events. The background events in this table were all subject to the generator-level selection criteria listed in Table II.

	$e^* \to e\gamma$			$e^* \to eZ$			$e^* \to \nu W$			NC DIS	CC DIS	Compton	$\gamma p \to X$
e^* Mass [GeV]	50	100	250	125	200	290	125	200	290				
After Preselection	99	100	100	99	99	99	87	86	84	95	83	10	27
After Fiducial l^* Cuts	80	94	93	80	94	95	77	76	71	11	48	1	3

TABLE IV. Acceptances, in percent, for ν^* events.

	$\nu^* \to e\gamma$			$\nu^* \to \nu Z$			$\nu^* \to eW$		
ν^* Mass [GeV]	50	100	250	125	200	250	125	200	250
After Preselection	99	100	100	95	91	87	99	100	100
After Fiducial l^* Cuts	90	90	85	90	80	76	97	98	97

TABLE V. Acceptances, in percent, for q^* events.

	$q^* \to q\gamma$		$q^* \to qZ$		$q^* \to qW$		$q^* \to qg$	
q^* Mass [GeV]	100	250	150	250	150	250	150	250
After Preselection	99	100	98	99	99	100	99	99
After Fiducial q^* Cuts	97	100	83	99	95	100	96	99

Both the preselection and the fiducial (l^* and q^*) cuts were highly efficient for selection of excited fermions while backgrounds due to deep inelastic scattering and photoproduction were strongly suppressed.

In addition to candidates for excited fermion decays, the two fiducial samples contained events from NC DIS, CC DIS, high E_T photoproduction, cosmic rays, and collisions of both the electron and proton beams with residual gas molecules in the beampipe. Using the HERA bunch structure, we estimated the size of some of these contributions. Counting the number of events from empty bunches we estimated that our sample contained less than 1% contamination from cosmic rays. Only 3 of the f^* decay channels studied had any surviving beam-gas or cosmic ray background events in the final sample (see Section VII), which were eliminated by visual scanning.

VII. ANALYSES

This section describes the selection procedure for the final data samples in each of the f^* decay modes. All analyses were based on the two fiducial data samples described in Section

VI and additional selection criteria were employed to select specific final state topologies. In all modes, summary tables list the cuts for quick reference.

Our background Monte Carlo samples (see Table II for luminosities) consisted of about 67,000 NC DIS events, 4,100 CC DIS events, 7,000 direct photoproduction events, and 18,000 resolved photoproduction events.

Approximately, 1000 Monte Carlo signal events were used in every channel. All the upper limits presented in this note are calculated at the 95% confidence level. A systematic uncertainty of 15% for the expected event rate (see Section VIII) is taken into account.

A. Excited Electrons

The Feynman diagram for excited electron production in ep scattering is shown in Figure 1. A second mechanism, the t-channel exchange of a virtual Z boson, is also included in HEXF. Monte Carlo studies showed that the inclusion of this mechanism represented only a 3.5% increase in production cross-section. We have searched for the decays: eγ, eZ, and νW. Details of the analysis are presented in the next three subsections.

1. $e^* \to e\gamma$

The decay of a heavy excited electron to a photon and an electron would leave a spectacular signature: two isolated energetic electromagnetic clusters and, if the proton dissociates, some hadronic energy around the forward beam pipe in an otherwise quiet detector. Possible backgrounds to this process include: (1) NC DIS events where a π^0 decay produces an energetic photon, and (2) high-energy elastic ($ep \to ep\gamma$) and inelastic Compton processes.

Starting with the fiducial l^* sample described earlier, events were first required to have two electromagnetic showers of which at least one had an angle less than 150^0 and an energy above 10 GeV. The other electromagnetic shower had to have an energy of at least 2 GeV.

Events were required to be contained within the detector by demanding 30 GeV$< \delta <$ 60 GeV. A total of 24 events passed these selection criteria. The distribution of the invariant $e\gamma$ masses is plotted in Figure 3 together with the results of a Monte Carlo study. None of the 24 events have an $e\gamma$ mass above 50 GeV. The number of candidate events as well as their mass distribution agrees well with our NC DIS Monte Carlo sample. In addition, one background event is expected from elastic Compton scattering at low invariant $e\gamma$ mass. The overall acceptance for this channel as a function of invariant $e\gamma$ mass is shown in Figure 4. The mass resolution for this channel as a function of invariant $e\gamma$ mass is shown in Figure 5. As a check on the sensitivity of the resolution to the overall energy scale (which determines the values of such variables as E_T and E_{EM}), the 150 GeV Monte Carlo sample was studied with a systematic energy shift of -3% and a Gaussian smearing of 5%. The resulting change in the width of the distribution was found to be 13%. Thus, the resolution is not strongly dependent on small variations in the energy scale.

No evidence for a resonance decaying to an $e\gamma$ final state is observed in the 1993 ZEUS data. Using an average detection efficiency of 80%, we obtained an upper limit on the production cross-section for an excited electron decaying to $e\gamma$ of 7.2 pb for invariant masses above 50 GeV. The $e^* \to e\gamma$ analysis is summarized in Table VI.

TABLE VI. Summary of the $e^* \to e\gamma$ analysis. Results are presented here for the invariant mass range $M_{e\gamma} > 50$ GeV. "Expected events" refers to the normalized number of events expected from the background Monte Carlo samples. "Average efficiency" is a measure of the percentage of Monte Carlo $e^* \to e\gamma$ events surviving the cuts over the studied mass range.

Cuts	$E_{EM\,1}$ >10 GeV, $\theta_{EM\,1}$ <150^0 30 < δ <60 GeV $E_{EM\,2}$ >2 GeV
Expected events with $M_{e\gamma} < 296$ GeV	27.1
Observed events with $M_{e\gamma} < 296$ GeV	24
Average efficiency	80%
Expected events with $M_{e\gamma} > 50$ GeV	2.7
Observed events with $M_{e\gamma} > 50$ GeV	0
$\sigma(ep \to e\gamma X)$ for $M_{e\gamma} > 50$ GeV	< 7.2 pb 95% C.L.

2. $e^* \to eZ$

Three decay modes of the Z boson were considered in the search for $e^* \to eZ$: (1) $Z \to e^+e^-$ (BR = 3.36%), (2) $Z \to q\bar{q}$ (BR = 69.9%), and (3) $Z \to \nu\bar{\nu}$ (BR = 20.0%) [16]. Due to its large branching ratio, the $q\bar{q}$ final state dominates our sensitivity in this channel.

Possible backgrounds to this process include: (1) NC DIS events where a radiated energetic gluon produces a second jet or where π^0 decays produce two energetic photons, and (2) CC DIS events where energetic π^0 decays produce an energetic photon. To search for all these modes, starting from the fiducial l^* sample, we required the event to have an electromagnetic shower with polar angle less than 125^0 and energy greater than 10 GeV. Additionally, for the decay modes without neutrinos, we required 30 GeV $< \delta <$ 60 GeV.

In the search for the first mode ($e^* \to eZ \to ee\bar{e}$) the data sample was further restricted by imposing the requirement of two additional electromagnetic clusters in the calorimeter, each with energy greater than 2 GeV. After requiring a minimum of 10 GeV in the most energetic electromagnetic shower found, there remained only 1 event with 3 electromagnetic showers. It has an invariant mass below 30 GeV, moreover, the highest energy pair of electromagnetic showers in this event is 22 GeV, inconsistent with a Z decay. Background Monte Carlo predicted one event from NC DIS.

The signature for the second mode ($e^* \to eZ \to eq\bar{q}$) is a single energetic electron accompanied by high E_T hadronic deposits in the calorimeter. We selected this event topology by requiring the hadronic transverse energy, $E_T^{hadronic}$ to be greater than 60 GeV. $E_T^{hadronic}$ is defined as the total calorimeter transverse energy excluding the cells from the FCAL inner ring and the highest energy electromagnetic shower. The distributions shown in Figure 6 demonstrate that this cut is efficient for $e^* \to eZ$ decays while substantially reducing the NC DIS background. Two events passed these cuts, in good agreement with the expected Monte Carlo background from NC DIS (4.7 events).

The third mode ($e^* \to eZ \to e\nu\bar{\nu}$) is characterized by a single energetic electron combined with a large transverse momentum imbalance. To select these events, we imposed a cut of $p_T > 15$ GeV. Since large apparent p_T is also characteristic of many beam-gas events produced upstream of the apparent vertex found from track reconstruction, it was also required that at least 70% of the p_T come from calorimeter cells not in the FCAL inner ring. Furthermore, momentum loss through the neutrino implies that δ will be less than twice the incident electron beam energy, so we suppressed NC DIS background by requiring $\delta < 50$ GeV. This left no candidate events while there was an expected background from NC DIS Monte Carlo of 0.7 events.

Using the energy and angle of the electron and assuming that the hadronic system has the mass of the Z, and that production is dominated by low $Q^2_{l^*}$ so that the final state has no net transverse momentum, the mass of the e^* candidates may be calculated using the formula:

$$M^2_{e^*} \equiv M^2_{eZ} = \frac{4E_e E_{EM} \cos^2 \frac{\theta_{EM}}{2} + M^2_Z}{1 - \frac{E_{EM}}{E_e} \sin^2 \frac{\theta_{EM}}{2}}$$

where E_e is the electron beam energy, and E_{EM} and θ_{EM} are the energy and polar angle of the e^* decay electron. We combine the decay modes mentioned above and found no evidence for a heavy resonance decaying to an eZ final state. The invariant eZ mass distributions for the two surviving data events and a signal and a background Monte Carlo sample are shown in Figures 7a and 7b.

We have investigated whether one could reconstruct the Z mass if a signal were present in the $q\bar{q}$ channel. Using our 125 GeV $e^* \rightarrow eZ$ Monte Carlo sample we show in Figure 8 the invariant mass of the hadron system calculated from the calorimeter energy deposits but excluding the tagged electron cluster and the cells from the FCAL inner ring. The reconstructed Z mass is seen to be narrow but shifted down by 13% from the nominal Z mass. This shift is due to missing energy from non-instrumented material as well as energy lost down the beam pipe and energy excluded in the inner FCAL ring.

The overall acceptance for this decay channel as a function of the e^* mass is shown in Figure 4. The mass resolution in this mode is shown as a function of e^* mass in Figure 5. Using an average acceptance of 60% and an expected background of 5.2 events, the 2 events correspond to an upper limit of 12.5 pb for the cross-section of e^* production in this channel above an eZ mass of 100 GeV.

The $e^* \rightarrow eZ$ analysis is summarized in Table VII.

3. $e^* \rightarrow \nu W$

We have searched for an excited electron decaying to νW with subsequent decay of the W boson to either $q\bar{q}'$ (B.R. = 67.8%) or $e\bar{\nu}$ (B.R. = 10.8%) [16]. Backgrounds to this process include CC DIS with either an energetic gluon which produces a second jet ($q\bar{q}'$ mode) or an energetic π^0 which produces a high energy electromagnetic shower ($e\bar{\nu}$ mode).

For the $q\bar{q}'$ mode, the only energy observable in the detector is due to the hadronic decay of the W. Since one would expect that the decay neutrino from a massive state would produce a large missing transverse momentum, we only considered those events from the fiducial l^* sample with a $p_{T\ miss}$ of at least 15 GeV. Since many beam-gas events have large $p_{T\ miss}$, we required at least 70% of the p_T to come from calorimeter cells not in the inner ring of the FCAL. We then required that the total invariant mass in the calorimeter ($M_{hadronic}$, calculated excluding cells in the inner ring of the FCAL) be at least 50 GeV, consistent with

TABLE VII. Summary of the $e^* \to eZ$ analysis. Results are presented here for the invariant mass range $M_{eZ} > 100$ GeV. "Expected events" refers to the normalized number of events expected from the background Monte Carlo samples. "Average efficiency" is a measure of the percentage of Monte Carlo $e^* \to eZ$ events surviving the cuts over the studied mass range.

Mode	Z$\to q\bar{q}$	Z$\to e^+e^-$	Z$\to \nu\bar{\nu}$
Cuts	$E_{EM\ 1}$ >10 GeV, $\theta_{EM\ 1}$ <125^0		
	30 < δ <60 GeV		δ <50 GeV
	$E_T^{hadronic}$ >60 GeV	$E_{EM\ 2}$ >2 GeV, $E_{EM\ 3}$ >2 GeV	$p_{T\ miss}$ >15 GeV $p_{T\ miss}^{inner\ ring}/p_{T\ miss}$ <0.7
Expected events	4.7	1.4	0.7
Observed events	2	1*	0
Average efficiency	49%	not used	11%
Total expected events	5.2 (with overlap)		
Total observed events	2		
Total average efficiency	60%		
Events with M_{eZ} > 100 GeV	2	0	0
$\sigma(ep \to eZX)$ for M_{eZ} > 100 GeV			< 12.5 pb 95% C.L.

*) Event has insufficient energy for Z decay.

the large mass expected from W decay. Only 11 events passed these cuts; 7 of these were identified by visual scanning as beam-gas events and 1 as a cosmic-ray event. This left 3 candidate events.

To select excited electron candidates decaying into νW followed by $W \to e\bar{\nu}$ we used cuts identical to those used in the $q\bar{q}'$ mode, except that now the cut on $M_{hadronic}$ was replaced by a requirement of an electromagnetic shower with more than 10 GeV and polar angle less than 125^0. One event survived these cuts, but was rejected by visual inspection as a beam-gas event. Expected NC DIS background in this mode was 0.7 events.

On combining these two decay modes, the acceptance with this selection is quite high for signal events (see Figure 4), while the backgrounds are substantially reduced. The mass resolution in this mode is shown as a function of e^* mass in Figure 5.

We first consider the case where the W decays into $q\bar{q}'$. Since the neutrino is not observed, it is necessary to reconstruct the neutrino parameters assuming that the decay products balance transverse momentum (it is assumed that production is dominated by low $Q^2_{l^*}$). Using the total transverse momentum (p_T) and δ (see Section III), and assuming that the hadronic system has the mass of the W, M_W, one can calculate the invariant mass of the decaying e^*:

$$M^2_{e^*} \equiv M^2_{\nu W} = \frac{4p^2_{T\ miss}E^2_e + 2E_e M^2_W(2E_e - \delta)}{\delta(2E_e - \delta)}.$$

The invariant νW mass distribution for the three remaining data events is shown in Figure 7d together with results from signal (shown in 7c) and background Monte Carlo simulations. From Monte Carlo calculations, one expects 1.6 background events from NC DIS and CC DIS in the final sample.

In the case where the W decays into νl, the assumption that the transverse momentum is balanced is no longer valid. Nevertheless, the mass distribution obtained by using the above formula is useful in discriminating signal from background. The high-mass tail observed in Figure 7 results from events of this type.

No evidence for a νW resonance is observed. Using an average acceptance of 60% and a background expectation of 1.6 events, the three observed events correspond to an upper limit of 21.9 pb for the cross-section of e^* production in this channel above a mass of 100 GeV. The $e^* \rightarrow \nu W$ analysis is summarized in Table VIII.

TABLE VIII. Summary of the $e^* \rightarrow \nu W$ analysis. Results are presented here for the invariant mass range $M_{\nu W} > 100$ GeV. "Expected events" refers to the normalized number of events expected from the background Monte Carlo samples. "Average efficiency" is a measure of the percentage of Monte Carlo $e^* \rightarrow \nu W$ events surviving the cuts over the studied mass range.

Mode	W $\rightarrow q\bar{q}'$	W $\rightarrow \bar{\nu}$e
Cuts	$\mathrm{p}_{T\ miss}$ >15 GeV $\mathrm{p}_{T\ miss}^{inner\ ring}/\mathrm{p}_{T\ miss}$ <0.7 δ <50 GeV	
	$M_{hadronic}$ >50 GeV	$E_{EM\ 1}$ >10 GeV, θ_{EM} <125^0
Expected events	1.6	0.7
Observed events	3	0
Average efficiency	53%	7%
Total expected events	1.6 (with overlap)	
Total observed events	3	
Combined efficiency	60%	
Events with $M_{\nu W} > 100$ GeV	3	
$\sigma(ep \rightarrow \nu W X)$ for $M_{\nu W} > 100$ GeV	< 21.9 pb 95% C.L.	

B. Excited Neutrinos

Excited neutrinos can be produced at HERA via exchange of W bosons. It should be noted that events produced by W exchange peak much less sharply at low Q^2_{l*} than γ propagator events. Thus there would often be a visible parton recoil jet associated with ν^* production. Events where the proton does not dissociate, which should be a major contribution to the e^* channels, are not possible in this channel.

1. $\nu^* \rightarrow \nu\gamma$

If the neutrino has charged subcomponents, decay of its excited state into $\nu\gamma$ is possible. Such an event would be characterized by missing p_T associated with the ν, a high energy electromagnetic shower associated with the γ, and (usually) a recoil jet from the quark struck by the W. Backgrounds to this process tend be concentrated at low values of $\mathrm{p}_{T\ miss}$ and to result from NC DIS.

Beginning with the fiducial l^* sample, we first required an electromagnetic shower with energy>10 GeV. The neutrino would lead to a non-zero $\mathrm{p}_{T\ miss}$ and to (δ) less than twice the incident electron beam energy. We therefore required $\mathrm{p}_{T\ miss}$ >15 GeV and δ <50 GeV. In addition, the total transverse energy E_T from both the γ and the recoil jet should be large, so we required $E_T > 40$ GeV. Monte Carlo studies yield efficiencies rising from 45% at ν^* mass of 50 GeV to 65% at 250 GeV, as shown in Figure 4. The mass resolution in this mode is shown as a function of ν^* mass in Figure 5. Expected backgrounds were 0.9 NC DIS events and less than 0.1 CC DIS events. No event remained after these cuts. This, combined with an average efficiency of 60% and an expected background of 0.9 events, corresponds to an upper limit of 9.6 pb for the cross-section of ν^* production and decay into $\nu\gamma$ above a mass of 50 GeV. The $\nu^* \to \nu\gamma$ analysis is summarized in Table IX.

TABLE IX. Summary of the $\nu* \to \nu\gamma$ analysis. Results are presented here for the invariant mass range $M_{\nu\gamma} > 50$ GeV. "Expected events" refers to the normalized number of events expected from the background Monte Carlo samples. "Average efficiency" is a measure of the percentage of Monte Carlo $\nu^* \to \nu\gamma$ events surviving the cuts over the studied mass range.

Cuts	E_{EM} >10 GeV δ <50 GeV $\mathrm{p}_{T\ miss}$ >15 GeV E_T >40 GeV
Expected events	0.9
Observed events	0
Average efficiency	60%
Events with $M_{\nu\gamma} > 50$ GeV	0
$\sigma(ep \to \nu\gamma X)$ for $M_{\nu\gamma} > 50$ GeV	< 9.6 pb 95% C.L.

2. $\nu^* \to \nu Z$

For ν^* production via W exchange, and followed by a decay into the final state νZ, the recoil jet can be used to assist in the design of efficient cuts. Monte Carlo studies showed that the recoil jet tends to have sufficient angle with respect to the heavy boson decay jets to give a large value for $M_{hadronic}$ (typically > 100 GeV). At low masses, where most of the ν^* energy is used in forming the heavy boson and little is left for the lepton, the requirement of a large $M_{hadronic}$ can replace the $\mathrm{p}_{T\ miss}$ requirement imposed on the lepton. This suggests the use of cuts excluding certain regions in the $M_{hadronic}$–$\mathrm{p}_{T\ miss}$ plane (see Figure 9).

Backgrounds to this process tend to come from CC DIS events with two or more jets having either fairly wide separation or large energies. To search for $\nu^* \to \nu$Z decay, we began with the fiducial l^* sample and required δ <50 GeV in order to account for the missing ν. Only events with $\mathrm{p}_{T\ miss} > 15$ GeV and hadronic mass > 50 GeV were accepted. However, as described above and demonstrated in Figure 9, the acceptance can be improved, while maintaining good background suppression, when the $\mathrm{p}_{T\ miss}$ requirement is relaxed to 5 GeV for events with hadronic masses above 125 GeV. To suppress beam-gas background, we accepted events only if at least 70% of the p_T comes from calorimeter cells not in the FCAL inner ring.

After the above cuts, 3 events remain, consistent with the background expectations of 2.6 NC DIS, 0.7 CC DIS, and 0.1 photoproduction events.

The mass formula for e^* in the νW decay mode was derived assuming that the transverse momentum of the e^* was zero. It is not a precise assumption in the presence of a recoil jet (as is often the case for ν^* production) but it is a good approximation which improves in accuracy as the ν^* mass increases. At low masses ($M_{\nu^*} = M_{e^*} = 100$ GeV), where the approximation is least accurate, Monte Carlo studies indicate that the ν^* reconstructed mass distribution is 4% higher and 36% wider than that of the e^*. Thus, assuming that the mass of the hadronic system is the Z mass, M_Z, the ν^* invariant mass is obtained from:

$$M^2_{\nu^*} \equiv M^2_{\nu Z} = \frac{4p^2_{T\ miss}E^2_e + 2E_e M^2_Z(2E_e - \delta)}{\delta(2E_e - \delta)}.$$

The acceptance for this decay channel is plotted in Figure 4 as a function of the ν^* mass. The mass resolution in this mode is shown as a function of ν^* mass in Figure 5. As a check on the sensitivity of the resolution to the value of the overall energy scale (which determines the values of $M_{hadronic}$ and $p_{T\ miss}$) we imposed a -3% shift and a Gaussian smearing of 5% on the energy scale for a 200 GeV ν^*. The resulting change in reconstructed width was less than 1%. Using an average efficiency of 65% and an estimated background of 3.4 events, the 3 observed events correspond to an upper limit of 15.6 pb for the cross-section of ν^* production in this channel above a νZ mass of 100 GeV. The $\nu^* \rightarrow \nu Z$ analysis is summarized in Table X.

TABLE X. Summary of the $\nu^* \rightarrow \nu Z$ analysis. Results are presented here for the invariant mass range $M_{\nu Z} > 100$ GeV. "Expected events" refers to the normalized number of events expected from the background Monte Carlo samples. "Average efficiency" is a measure of the percentage of Monte Carlo $\nu^* \rightarrow \nu Z$ events surviving the cuts over the studied mass range.

Cuts	δ <50 GeV $M_{hadronic}$ >50 GeV $p_{T\ miss}$ >5 GeV ($p_{T\ miss}$ >15 GeV) .or. ($M_{hadronic}$ >125 GeV) $p_{T\ miss}^{inner\ ring}/p_{T\ miss}$ <0.7
Expected events	3.4
Observed events	3
Average efficiency	65%
Events with $M_{\nu Z} > 100$ GeV	3
$\sigma(ep \rightarrow \nu ZX)$ for $M_{\nu Z} > 100$ GeV	< 15.6 pb 95% C.L.

3. $\nu^* \rightarrow eW$

As for the $e^* \rightarrow eZ$ case, we searched for the W boson in the hadronic ($q\bar{q}'$) and the electronic ($e\nu$) decay modes. (It is worth noting that some decays from other modes should also survive our cuts.) Backgrounds to this process are similar to the $e^* \rightarrow eZ$ mode. For the hadronic W decay mode we began with the fiducial l^* sample and required the event to be contained in the detector (30 GeV< δ <60 GeV). A successful candidate had to contain an electromagnetic cluster with more than 10 GeV energy and a polar angle less than 125^0. As for the $e^* \rightarrow \nu W$ analysis, we required that the hadronic transverse energy, excluding cells from the inner FCAL ring, be at least 60 GeV. To account for the undetected neutrino, we selected candidate events for the $\nu^* \rightarrow eW \rightarrow ee\nu$ decay chain by requiring $\delta < 50$ GeV and imposing a $\mathrm{p}_{T\ miss} > 15$ GeV cut. To suppress beam-gas background, we accepted events only if at least 70% of the $\mathrm{p}_{T\ miss}$ comes from calorimeter cells not in the FCAL inner ring. No event survived these selection criteria, while the expected background is 0.7 NC DIS and 0.1 CC DIS events. Combining both W decay modes, we found 2 candidate events with an expected background of 5.2 NC DIS and 0.1 CC DIS events.

The assumption that only the excited fermion decay products carry E_T, which is used in deriving the mass formula for the analogous e^* mode, is only approximately correct, but the E_T carried by the recoil jet represents only a small effect. Therefore, with the assumption that the hadronic system has the mass of the W, the ν^* mass is calculated using the formula:

$$M_{\nu^*}^2 \equiv M_{eW}^2 = \frac{4E_e E_{EM} \cos\frac{\theta_{EM}}{2}^2 + M_W^2}{1 - \frac{E_{EM}}{E_e} \sin\frac{\theta_{EM}}{2}^2}$$

where the electron comes from ν^* decay. Figure 4 shows the detector acceptance for this decay channel as function of the ν^* mass. The mass resolution in this mode is shown as a function of ν^* mass in Figure 5. Using an average efficiency of 60% and an estimated background of 5.2 events, the 2 observed events correspond to an upper limit of 12.5 pb for the cross-section of ν^* production and decay into eW above a mass of 100 GeV. The $\nu^* \rightarrow eW$ analysis is summarized in Table XI.

C. Excited Quarks

Except for the relatively small fraction of heavy-boson decays containing neutrinos, all excited quark decay modes ($q\gamma$, qW, qZ, and qg) should balance p_T. Only those events of the fiducial q^* sample for which the transverse momentum was less than 40 GeV were considered for further analysis.

Additionally, all excited quark decay modes have energetic hadronic showers in the final state producing a characteristic signature of large transverse energy in the detector. In calculating E_T, a cone around the beam pipe of half-angle 9.2° ($E_T^{\theta<9.2}$) was excluded for $q^* \rightarrow q\gamma$ while a cone of half-angle of 18.3° was excluded for the analyses of the other final states. These cone cuts effectively remove beam-gas, photoproduction and DIS backgrounds. We found good agreement between data and the background calculation. Monte Carlo studies suggest that a strong E_T cut would reduce the background while maintaining high efficiency for signal events. Thus, events with transverse energy ($E_T^{\theta<9.2}$) greater than 70 GeV were selected. Photoproduction background was further reduced by requiring $\delta > 20$ GeV.

TABLE XI. Summary of the $\nu^* \rightarrow eW$ analysis. Results are presented here for the invariant mass range $M_{eW} > 100$ GeV. “Expected events” refers to the normalized number of events expected from the background Monte Carlo samples. “Average efficiency” is a measure of the percentage of Monte Carlo $\nu^* \rightarrow eW$ events surviving the cuts over the studied mass range.

Mode	W $\rightarrow q\bar{q}'$	W $\rightarrow \bar{\nu}$e
Cuts	$E_{EM\ 1}$ >10 GeV, θ_{EM} <125^0	
	30< δ <60 GeV	δ <50 GeV
	$E_T^{hadronic}$ >60 GeV	$\mathrm{p}_{T\ miss}$ >15 GeV
		$\mathrm{p}_{T\ miss}^{inner\ ring}/\mathrm{p}_{T\ miss}$ <0.7
Expected events	4.7	0.8
Observed events	2	0
Average efficiency	43%	17%
Total expected events	5.3	
Total observed events	2	
Combined efficiency	60%	
Events with $M_{eW} > 100$ GeV	2	
$\sigma(ep \rightarrow eWX)$for $M_{eW} > 100$ GeV	< 12.5 pb 95% C.L.	

1. $q^* \rightarrow q\gamma$

Starting from the data sample defined above we selected candidates for the decay $q^* \rightarrow q\gamma$ by requiring an electromagnetic cluster with energy greater than 50 GeV and no matching tracks in the central tracking detector. After these cuts, one event remained, while background Monte Carlo predicted 1.2 events. The $q\gamma$ invariant mass value calculated from the energy deposited in the calorimeter for this candidate as well as for a signal (see Figure 10c) and a background Monte Carlo sample are shown together with data in Figure 10d. No evidence is seen for q^* production in this data sample. Backgrounds to this process include NC DIS with both high E_T and a poorly matched track, and photoproduction with both high E_T and a high energy π^0 which mimics a γ.

In Figure 4, we plot the acceptance for this analysis as a function of the $q\gamma$ invariant mass. The mass resolution in this mode is shown as a function of q^* mass in Figure 5. The efficiency is close to 70% over most of the mass range; the inefficiency at low $q\gamma$ masses is caused by the δ cut.

Using an average detection efficiency of 70% and an expected background of 1.2 events, the single candidate event corresponds to an upper limit of 11.3 pb for the cross-section of q^* production and subsequent decay to $q\gamma$ above a $q\gamma$ mass of 100 GeV. The $q^* \rightarrow q\gamma$ analysis is summarized in Table XII.

2. $q^* \rightarrow qZ,\ q^{'}W,\ qg$

In the search for excited quarks decaying to qZ or $q^{'}W$ we concentrated on the hadronic decay modes of the heavy bosons. Thus, excited quarks decaying to either qZ, $q^{'}W$, or qg are characterized by hadronic jets in the final state. Since we make no attempt to isolate jets

TABLE XII. Summary of the $q^* \rightarrow q\gamma$ analysis. Results are presented here for the invariant mass range $M_{q\gamma} > 100$ GeV. "Expected events" refers to the normalized number of events expected from the background Monte Carlo samples. "Average efficiency" is a measure of the percentage of Monte Carlo $q^* \rightarrow q\gamma$ events surviving the cuts over the studied mass range.

Cuts	p_T <40 GeV $E_T^{\theta>9.2^0}$ >70 GeV δ >20 GeV (E_{EM} >50 GeV) $\cdot$ (No matched track)
Expected events	1.2
Observed events	1
Average efficiency	70%
Events with $M_{q\gamma} > 100$ GeV	1
$\sigma(ep \rightarrow q\gamma X)$ for $M_{q\gamma} > 100$ GeV	< 11.3 pb 95% C.L.

in this analysis, these three final states are indistinguishable and will be treated together. Backgrounds to this process tend to come from both NC DIS and photoproduction events with large E_T without a well isolated electromagnetic shower.

To produce a heavy object at low Q_l^2 (the data are dominated by low Q_l^2 processes), the energy transfer from the incident electron to the virtual gauge boson has to be large. Therefore we would expect only low energy scattered electrons in our final sample. We did not attempt to reconstruct this electron since, in most cases, it disappears down the beam pipe. However, we searched for isolated energetic electrons to tag background from neutral current DIS. Events were accepted if they did not contain an isolated electromagnetic shower with energy of more than 10 GeV. An electron was defined as isolated if it had less than 5 GeV associated hadronic energy within a cone of 40^0. Two events survived this cut while background Monte Carlo calculations predicted 2.6 events. The invariant mass distribution, obtained by summing over all calorimeter cells, is shown in Figures 10a and 10b together with distributions from signal and background Monte Carlo samples. No evidence is seen for q^* decaying into these hadronic final states. The acceptances and widths for these decay channels are plotted in Figures 4 and 5. The mass resolution in this mode is shown in Figure 5 as a function of the generated q^* mass. Using an average efficiency of 40% and an estimated background of 2.6 events, the 2 observed events correspond to an upper limit of 23.0 pb for the cross-section of q^* production and decay to qg, $q^{'}W$, or qZ above a mass of 100 GeV. The $q^* \rightarrow qg$ (Z, W) analysis is summarized in Table XIII.

VIII. EVALUATION OF SYSTEMATIC UNCERTAINTIES

In our determination of the systematic error, we distinguish between experimental and theoretical uncertainties.

TABLE XIII. Summary of the $q^* \rightarrow qg$, $q^{'}W$, qZ analysis. Results are presented here for the invariant mass range $M_{q^*} > 100$ GeV. "Expected events" refers to the normalized number of events expected from the background Monte Carlo samples. "Average efficiency" is a measure of the percentage of Monte Carlo $q^* \rightarrow qg$, $q^{'}W$, qZ events surviving the cuts over the studied mass range.

Cuts	$p_T <40$ GeV $E_T^{\theta>18.3^0} >70$ GeV $\delta >20$ GeV No isolated $E_{EM} > 10$ GeV
Expected events	2.6
Observed events	2
Average efficiency	40%
Events with $M_{q^*} > 100$ GeV	2
$\sigma(ep \rightarrow \text{jets})$ for $M_{q^*} > 100$ GeV	< 23.0 pb 95% C.L.

A. Experimental Systematic Uncertainties

Experimental systematic errors on the derived cross sections are introduced by the luminosity measurement and the particular reconstruction procedure chosen for the analysis. The systematic error on measurement of the integrated luminosity, $\mathcal{L}$, is 3.3% [23].

The uncertainties in the CC and NC samples can be divided into the following contributions: (1) vertex reconstruction efficiency, (2) electron identification efficiency, and (3) effects of energy scale uncertainty on the total acceptance. The error on the vertex reconstruction efficiency was estimated by repeating the analysis with different vertex reconstruction algorithms. This yielded an uncertainty of 6% in the efficiency. The uncertainty in the electron identification was estimated both by using alternate electron finding algorithms, and varying cuts within the standard electron identification algorithm for both data and Monte Carlo. This yielded an uncertainty on the electron identification efficiency of 4%. The effects of the overall energy shift, relevant to the δ, E_T, $p_{T\ miss}$, $M_{hadronic}$ cuts and the cuts on the lepton energy, were less than 3%.

By systematically varying the cuts in the three excited fermion analyses, we estimated what systematic effect is introduced by their values. This uncertainty in the efficiency was found to be less than 4%.

The calculation of the upper limit curves for the excited fermion production cross-section requires a smooth parameterization of the acceptance as a function of the excited fermion mass. The interpolation between generated Monte Carlo mass points introduced an additional uncertainty of 5%.

Under the assumption that the various systematic errors are uncorrelated, we added the contributions in quadrature and determined the experimental systematic error to 11%.

B. Theoretical Uncertainties

The predicted f^* production cross-sections vary according to the model used. The application of radiative corrections to an expressly nonrenormalizable “effective Lagrangian” model is somewhat problematic. However, once a particular model was chosen, we could estimate the uncertainties introduced by radiative corrections and the parton density distributions used to model the proton. We estimated this contribution to be 8%. On comparing excited fermion Monte Carlo samples generated with decay distributions isotropic in the center of mass to those where the decay lepton distribution follows $1+\cos\theta$ (as predicted in the models of [3] [4]) the reconstruction efficiencies differed by less than 6%.

Combining these contributions in quadrature with the experimental uncertainties, we found the total systematic uncertainty to be 15%.

C. High energy Compton scattering

Since Compton scattering, $ep \to ep\gamma$, is topologically similar to an excited electron decaying to $e\gamma$, its analysis is a systematic check of the $e^* \to e\gamma$ analysis. As Compton events are concentrated at low E_T, and deposit energy mainly in the rear detector, to increase the sample size, starting before the level of the initial selection cuts, we modified the analysis criteria used in the $e^* \to e\gamma$ analysis. We selected events with exactly two electromagnetic clusters between polar angles of 85° and 165° with energies above 4 GeV. The range of allowed vertex z positions was widened to -75 cm $< z <$75 cm and the cut on δ was changed to $\delta > 35$ GeV. Additionally, we required 95% of the event's energy to come from the electromagnetic section of the calorimeter. Figure 11 shows agreement between the data and Monte Carlo, confirming our understanding of both the detector behaviour and the background sources.

IX. LIMIT PROCEDURE

A. Model Independent Limits

Since no evidence was observed for excited fermions in any of the above channels, we set cross-section limits for the production of the various fermion gauge boson final states. In so doing, the integrated luminosity and masses of the candidate events were taken from the data, and we obtained acceptances, mass resolutions, and background distributions from Monte Carlo calculations. The mass peaks from Monte Carlo models were fit with Gaussian lineshapes which were used to extract acceptances, $\epsilon(M)$, as functions of excited fermion masses. In the previous sections we have quoted limits on cross-sections averaged over a wide mass range. Figure 12 shows the upper limits on the cross-sections as functions of final state mass for each decay channel. Note that these curves are independent of the production mechanism. They were derived from the expression:

$$\sigma_{U.L.}(M_{f^*}) = \frac{N_{U.L.}(M_{f^*})}{\epsilon(M_{f^*})\mathcal{L}}. \tag{1}$$

Here M_{f^*} is the invariant mass of the final state under consideration, and $N_{U.L.}$ is the mass-dependent 95% upper limit on the number of events observed after accounting for systematic errors. In each channel, $N_{U.L.}$ is determined using Poisson statistics from the number of events observed, and the expected number of background events (from Monte Carlo) [24]. Detector resolution effects, as well as a systematic error of 15% (see Section VIII), were included in the calculation of $N_{U.L.}$.

To obtain the mass dependence of the detector acceptance for signal events, $\epsilon(M_{f^*})$, Monte Carlo data were generated for each of the excited lepton and quark decay chains for several f^* invariant masses between 50 GeV and 290 GeV. For each decay chain, the acceptance, the reconstructed signal width, and the reconstructed mean value for the resonance mass were parameterized by third order polynomial fits to the results obtained by the Monte Carlo study. To account for phase space effects near thresholds (such as the case of a low f^* candidate mass in a heavy boson decay mode), the polynomial was multiplied by a threshold factor of $\sqrt{M - M_0}$ where M_0 is the mass at threshold. This acceptance included contributions from geometry and detector inefficiencies, as well as the branching ratios for the heavy gauge boson decay channels studied.

B. Limits on Couplings and Compositeness Scale

To set limits on the f^* couplings, one needs to use a specific theoretical model. In an effective Lagrangian model of excited fermion production, one assumes spin-$\frac{1}{2}$ excited fermions are produced and decay through magnetic transitions mediated by the gauge bosons γ, Z, and W [3] [4]. The cross-section can be written quite generally as (see appendix):

$$\sigma(ep \to f^* X) = \frac{|c_{ef^*V}|^2 + |d_{ef^*V}|^2}{\Lambda^2} \sigma_0(M_{f^*}) \tag{2}$$

where c and d are the vector and axial vector coupling constants, Λ is the compositeness scale, V denotes the gauge boson exchanged, and M_{f^*} is the mass of the excited fermion. The "reference cross-section", σ_0, is dependent only on the kinematics of the final state and therefore completely defined by M_{f^*} (we expect that only one type of gauge boson exchange contributes significantly to the production cross-section). The decay width of each excited lepton is a function of c_{ff^*V} and d_{ff^*V}. Depending on the various c_{ff^*V} and d_{ff^*V} values, almost any channel may dominate the cross-section, though the couplings to the electron must remain significant if the state is to be produced with significant cross section. If one assumes that the couplings between the standard model fermions and their excited states are $SU(3) \otimes SU(2) \otimes U(1)$ symmetric, the 18 different vector and axial vector couplings (ignoring different quark flavours and mixing) can be written as functions of three couplings f, f', and f_s for $U(1)$, $SU(2)$ and $SU(3)_{colour}$, respectively. It is often assumed that c and d are equal. To maintain generality, we avoided making this additional assumption in deriving upper limits. This introduces a factor of $\sqrt{2}$ which must be accounted for in comparing our limits to some other publications [5] [25].

For excited electrons and quarks with masses below 225 GeV, the dominant contribution to the lineshape is the detector resolution. At higher masses, the intrinsic width increases as the coupling limit weakens due to the rapid decrease in σ_0 and the narrow-width approximation used in the calculation of $\sigma_0(m_{f^*})$ (see appendix) becomes questionable. For excited neutrinos, the smaller coupling limit implies that the width is large at even lower masses. Therefore, we present excited neutrino limits only for masses below 180 GeV. A similar argument could be made in the case of excited quarks where decay through gluons might be expected to cause the q^* width to be significantly larger than the width of excited leptons. HERA is only sensitive to q^* production via electroweak couplings, but we have also considered the possibility of q^* decay through gluons. It should be noted that q^* limits in the qg mode become questionable at higher masses if the q^* decay coupling to gluons is large. Evidence from other experiments, (see discussion and references in Section X) which give limits on q^* production via hadronic coupling, suggests that this is unlikely.

C. Limit Parameterization

Experimentally, the upper limit on the production cross-section of excited fermions is given by Equation 1. If we include the decay of the excited fermion to a particular final state this can be written as:

$$\sigma_{U.L.}(ep \to f^* X) \; = \; \frac{N_{U.L.}(M_{f^*})}{BR(f^* \to f'V)\; \epsilon(M_{f^*})\; \mathcal{L}} \tag{3}$$

where $BR(f^* \to f'V)$ is the branching ratio for a excited fermion f^* decaying to a fermion f' and a gauge boson V.

Combining Equation 3 with Equation 2 results in the following expression for the limit on the ratio of the sum of the coupling constants times the branching ratio:

$$\frac{(|c|^2 + |d|)^2}{\Lambda^2} BR(f^* \to f'V) = \frac{N_{U.L.}(M_{f^*})}{\sigma_0(M_{f^*})\; \epsilon(M_{f^*})\; \mathcal{L}}. \tag{4}$$

The 95% confidence level upper limits on the quantity $\sqrt{BR(f^* \to f'V)(|c|^2 + |d|^2)/\Lambda^2}$ are shown in Figures 13 - 15 for the various decay channels studied. The sensitivity to excited neutrino couplings is weaker (by approximately an order of magnitude) than that for e^* and q^* couplings due to the absence of a low Q^2_{l/l^*} singularity in the t-channel. Possible contributions of Z exchange effects to e^* and q^* production would be of similar magnitude. Differences in sensitivity among final states available to the different excited fermions arise from differences in the number of candidate events, acceptances, and branching ratios for the subset of gauge boson final states observed.

In calculating the limits, the systematic error (see Section VIII) was accounted for by increasing the value of $N_{U.L.}(M_{f^*})$ by 15%. Deviations of systematic errors from Gaussian behaviour due to independent contributions to the normalization (e.g. those of luminosity and acceptance) were assumed to be negligible. In addition, the systematic error on the normalization of the background and signal contributions was assumed to be 100% correlated.

X. DISCUSSION AND RESULTS

To place our results in the context of existing limits, we first discuss the findings of other searches. Limits on excited electrons due to searches for spacelike exchange contributions come from experiments at lower energies [26] [27]. Direct searches performed by the four LEP experiments [25] exclude excited fermions with masses below $M_Z/2$ and limit the coupling strengths below the Z mass. Searches at LEP for t-channel exchanges of excited electrons set limits on the coupling strength for excited electron masses as high as 116 GeV [25].

A result from the UA2 collaboration [28] puts limits on q^* production in $p\bar{p}$ collisions for masses below 288 GeV. A recent result from the CDF collaboration [29] sets an upper limit on excited quark production for masses which are below 540 GeV. Note that these limits only hold for the special case of q^* production via the gluon coupling, $qg \rightarrow q^*$. The limits given in this paper are complementary since at a $p\bar{p}$ collider excited quark production is dominated by the quark gluon coupling while at HERA we can investigate the electroweak couplings of excited quarks.

First results from the HERA experiments, based on an integrated luminosity of approximately 26 nb^{-1}, restrict excited electron and excited neutrino production for masses below 225 GeV [5] [6]. A new result from H1 reports limits similar to those shown here only for excited lepton searches [30]. This paper reports on new limits for l^* production and on the first search for q^* production at HERA.

No evidence for a heavy particle decaying to a final state comprised of a gauge boson and a fermion was observed in the 1993 ZEUS data sample. Even with relatively small integrated luminosity, we set stringent limits on excited fermion production. This is due to the large centre of mass energy of HERA and the almost 4π coverage of the ZEUS detector. This analysis is not background limited. At current luminosities, backgrounds have been controlled using only simple cuts; for example, we have not used track matching requirements in all channels or attempted to reconstruct heavy bosons.

Limits on the production cross sections for massive particles decaying to final states of gauge bosons and fermions are presented in Table XIV and Figure 12. We exclude, at the 95% confidence level, the production of a heavy resonance decaying to an electron and a photon with a cross section at the level of 7 to 23 pb. We have achieved stringent limits in the ν^* and q^* channels and improved our limits in the e^* channels by more than a factor of 4 over the first analyses at HERA [5] [6].

TABLE XIV. Summary of excited fermion detection efficiencies, observed candidates, expected backgrounds, and cross section limits (at the 95% confidence level) for masses below $\sqrt{s}$ =296 GeV.

Excited Fermion	Observed Events	Expected Events	Average Efficiency (%)	Cross Section (pb)
$e^* \rightarrow e\gamma$ $M_{e\gamma} > 50$ GeV	0	2.7	80	< 7.2
$e^* \rightarrow eZ$ $M_{eZ} > 100$ GeV	2	5.2	60	< 12.5
$e^* \rightarrow \nu W$ $M_{\nu W} > 100$ GeV	3	1.6	60	< 21.9
$\nu^* \rightarrow \nu\gamma$ $M_{\nu\gamma} > 50$ GeV	0	0.9	60	< 9.6
$\nu^* \rightarrow \nu Z$ $M_{\nu Z} > 100$ GeV	3	3.4	65	< 15.6
$\nu^* \rightarrow eW$ $M_{eW} > 100$ GeV	2	5.3	60	< 12.5
$q^* \rightarrow \gamma q$ $M_{q\gamma} > 100$ GeV	1	1.2	70	< 11.3
$q^* \rightarrow$ jets $M_{q^*} > 100$ GeV	2	2.6	40	< 23.0

ACKNOWLEDGEMENTS

We thank the DESY directorate for their strong support and encouragement. The experiment was made possible by the inventiveness and diligent efforts of the HERA machine group who continued to run HERA most efficiently during 1993. We also gratefully acknowledge the support of the DESY computing and network services.

Appendix

Theoretical Models and Cross-Sections

1. Excited Lepton Production

We use specific theoretical models in order to calculate efficiencies for the signal, as well as to set limits on the ratios of the couplings to the compositeness scale. For excited leptons, we used the model of Hagiwara et al [3]. In this particular model, the excited fermions have spin and weak isospin 1/2. The (magnetic) transitions between excited and ordinary fermions, are mediated by the gauge bosons γ, Z and W. The production of excited fermions is then described in the framework of an effective Lagrangian [3]

$$\mathcal{L}_{eff} = \sum_{V=\gamma,Z,W} \frac{e}{\Lambda} \overline{F} \sigma^{\mu\nu} (c_{VFf} - d_{VFf}\gamma_5) f \partial_\mu V_\nu \quad + \quad h.c. \tag{5}$$

where F and f denote the excited and ordinary fermions and V is the boson to which the f and F couple. The compositeness scale, Λ, describes the strength of the binding of the new constituent particles. Hagiwara et al. also assume that the excited leptons form left-handed and right-handed doublets. These assumptions arise from the fact that the low energy limit of new physics at high energies should not distort the $SU(3) \otimes SU(2) \otimes U(1)$ symmetries of the standard model.

The coupling constants c_{VFf} and d_{VFf} are further constrained by $(g-2)$ experiments through high-precision measurements of the magnetic moment and by the absence of an electric dipole moment for the electron.

Based on the effective Lagrangian, the differential production cross-section for $ep \to f^* X$ can be calculated. To model $ep \to f^* X$, the proton was assumed to supply a parton q with density $\mathcal{H}_q(x, Q^2_{l/l^*})$. As an example (see [3] for details), we present the differential cross-section for the production of e^*'s via photon exchange:

$$\frac{d^2\sigma}{dx dQ^2_{l^*}} = \sum_q x\mathcal{H}_q(x, Q^2_{l^*}) \frac{d\sigma(eq \overset{\wedge}{\rightarrow} e^* X)}{dQ^2_{l^*}} \tag{6}$$

where $x\mathcal{H}_q(x, Q^2_{l^*})$ is the parton (quark) momentum density. The parton cross section can be written as

$$\frac{d\hat{\sigma}}{dQ^2_{l^*}} = \frac{2\pi\alpha^2 \mathcal{Q}_f^2 (|c|^2 + |d|^2)}{\Lambda^2 \hat{s}^2 Q^2_{l^*}} [2\hat{s}^2 - (Q^2_{l^*} + M^2_{l^*}) \cdot (2\hat{s} - M^2_{l^*})]. \tag{7}$$

The $\mathcal{Q}_f$ represents the quark charge and $\hat{s} = xs$.

Once produced, the excited lepton can decay into standard fermions and gauge bosons. In this analysis, we considered:

$$e^* \to e\gamma,\ eZ,\ \nu W$$

$$\nu^* \to \nu\gamma,\ \nu Z,\ eW.$$

The branching ratio for a particular mode was calculated from:

$$\mathrm{BR}(\mathrm{l}^* \to \mathrm{lV}) = \frac{,\,(\mathrm{l}^* \to \mathrm{lV})}{,\,(\mathrm{Total})}. \tag{8}$$

Within this model, the decay width of the excited lepton is a function of c and d and is given by the expression:

$$,\,(l^* \to lV) = \frac{\alpha}{2}\frac{M_*^3}{\Lambda^2}(|c_{VfF}|^2 + |d_{VfF}|^2)(1 - \frac{M_V^2}{M_*^2})^2(1 + \frac{m_V^2}{2M_*^2}). \tag{9}$$

The Lagrangian describing the transition between excited fermions and ordinary fermions should respect chiral symmetry in order to protect the light leptons from acquiring a large anomalous magnetic moment which is ruled out by experiment [26] [31]. This means that only the right-handed part of the excited fermions takes part in the magnetic de-excitation. The latter is described in an $SU(2)\otimes U(1)$ invariant form by the following effective Lagrangian which can be derived from Equation 5 under the above assumptions.

$$\mathcal{L}_{ff^*} = \frac{1}{2\Lambda}\bar{F}\sigma^{\mu\nu}[gf\frac{\vec{\tau}}{2}\vec{W}_{\mu\nu} + g'f'\frac{Y}{2}B_{\mu\nu}]f_L + h.c. \tag{10}$$

where g and g' are the usual weak coupling constants: $g = e/\sin\theta_W$ and $g' = e/\cos\theta_W$, where e is the electron charge and $\sin\theta_W^2 = 1 - \cos\theta_W^2 = \sin^2\theta_W = 0.231$ [16]. The factors f and f' are associated with the two gauge groups and parameterise two different scales Λ/f and Λ/f' for the two groups $SU(2)$ and $U(1)$. In this model, the coupling constants satisfy $c_{fVf^*} = d_{fVf^*}$ and more specifically they can be written in terms of f and f' as:

$$c_{\gamma e^* e} = \frac{-1}{4}(f + f') \tag{11}$$

$$c_{Ze^* e} = \frac{-1}{4}(f\cot\theta_W + f'\tan\theta_W) \tag{12}$$

$$c_{W^- e^* \nu} = \frac{f}{2\sqrt{2}\sin\theta_W} \tag{13}$$

$$c_{\gamma\nu^*\nu} = \frac{-1}{4}(f - f') \tag{14}$$

$$c_{Z\nu^*\nu} = \frac{-1}{4}(f\cot\theta_W - f'\tan\theta_W) \tag{15}$$

$$c_{W^+\nu^* e} = \frac{f}{2\sqrt{2}\sin\theta_W}. \tag{16}$$

Under the assumption $c_{fVf^*} = d_{fVf^*}$, limits on compositeness of fermions are sometimes given as function of $c/\Lambda \times \mathrm{BR}$. To be compared to the results presented in Figures 13 - 15 these limits have to be multiplied by $\sqrt{2}$.

2. Excited Quark Production

To model excited quark production and decay we have used the models of Boudjima et al. and of Baur et al. [4] which are extensions of the model of Hagiwara et al. [3]. In this model, the effective Lagrangian given in Equation 10 is extended to include the strong interaction:

$$\mathcal{L}_{ff^*} = \frac{1}{2\Lambda}\overline{F}\sigma^{\mu\nu}[gf\frac{\vec{\tau}}{2}\vec{W}_{\mu\nu} + g'f'\frac{Y}{2}B_{\mu\nu} + g_s f_s\frac{\vec{\lambda}}{2}\vec{G}_{\mu\nu}]f_L + h.c. \tag{17}$$

In ep scattering, excited quarks could be produced by exchange of the gauge bosons, as a quark–excited quark pair in photon-gluon fusion or in a resolved photoproduction process. These second and third classes of processes are expected to be negligible because of the soft gluon distribution in both the proton and the photon. With this assumption, the production cross-section calculation is very similar to that for excited leptons up to corrections for the proton mass. Photon exchange dominates this process.

Once produced, the excited quark can decay either through the weak or strong interactions. In this analysis we have included the following decay final states:

$$q^* \rightarrow q\gamma,\ qZ,\ q^{'}W,\ qg.$$

REFERENCES

[1] F. E. Low, Phys. Rev. Lett. 14 (1965) 238.

[2] W. Buchmüller, 24th. Int. Universitätswoche für Kernphysik, Schladmig Austria, February 1985; R. Peccei, Proceedings of the Lake Louise Winter Institute, Lake Louise Canada, February 1987; F. Boudjema, Int. J. Mod. Phys. A6 (1991) 1; I. A. D'Souza and C. S. Kalman *Preons: Models of Leptons, Quarks and Gauge Bosons as Composite Objects*, World Scientific, Singapore, (1992) ISBN 981-02-1019-1.

[3] K. Hagiwara, S. Komamiya and D. Zeppenfeld, Z. Phys. C29 (1985) 115.

[4] U. Baur, M. Spira, and P. M. Zerwas, Phys. Rev. D42 (1990) 815; F. Boudjema, A. Djouadi, J.L. Kneur, Z. Phys. C57 (1993) 425; F. Schrempp, DESY 93-096.

[5] H1 Collaboration, I. Abt *et al.*, Nucl. Phys. B396 (1993) 3.

[6] ZEUS Collaboration, M. Derrick *et al.*, Phys. Lett. B316 (1993) 207.

[7] ZEUS Collaboration, M. Derrick *et al.*, Phys. Lett. B303 (1993) 183; ZEUS Collaboration, M. Derrick *et al.*, Phys. Lett. B293 (1992) 465; ZEUS Collaboration, M. Derrick *et al.*, Phys. Lett. B297 (1992) 404.

[8] C. B. Brooks *et al.*, Nucl. Inst. and Meth. A283 (1989) 477; B. Foster *et al.*, Nucl. Inst. and Meth. A338 (1994) 185.

[9] A. Andresen *et al.*,

[10] R. Brun *et al.*, GEANT 3.13, CERN DD/EE/84-1 (1987).

[11] H. J. Kim and S. Kartik, LSU Preprint, LSUHE-145-1993.

[12] Ch. Berger and W. Wagner, Phys. Rep. 146, (1987) 1.

[13] A. D. Martin, R. G. Roberts and W. J. Stirling,

[14] M . Bengtsson, G. Ingelman and T. Sjöstrand, Nucl. Phys. B 301 (1988) 554.

[15] T. Sjöstrand, JETSET 6.3, Comput. Phys. Commun. 39 (1986) 347.

[16] Review of Particle Properties, L. Montanet *et al.*, Phys. Rev. D50 (1994).

[17] A. Kwiatkowski, H. Spiesberger and H.-J. Möhring, HERACLES 4.1, Proc. Workshop on Physics at HERA, Vol. 3, DESY (1992);

[18] B. Andersson *et al.*,

[19] L. Lönnblad, ARIADNE 3.1, Comput. Phys. Commun. 71 (1992) 15.

[20] T. Carli *et al.*," Physics at HERA" (proceedings), Hamburg, October (1991) 1468.

[21] G. Marchesini *et al.*, HERWIG 5.6, Comput. Phys. Commun. 67 (1992) 465.

[22] The ZEUS Detector, Status Report 1993, ed. U. Holm, DESY 1993.

[23] ZEUS Collaboration, M. Derrick *et al.*, DESY-94-143 (1994).

[24] K. W. McLean, DESY-F15-90-03, (1990).

[25] ALEPH Collaboration, D. Decamp *et al.*, Phys. Rep. 216 (1992) 253.; DELPHI Collaboration, P. Abreu *et al.*, Z. Phys. C53 (1992) 41; L3 Collaboration, O. Adriani *et al.*, Phys. Lett. B288 (1992) 404; OPAL Collaboration, M.Z. Akrawy *et al.*, Phys. Lett. B257 (1991) 531; M. Bardadin-Otwinowska, Z. Phys. C55 (1992) 163, and references therein; J. C. Montero and V. Pleitez, Phys. Lett. B321 (1994) 267 and references therein; H. Janssen, Part. World, vol. 3, no. 4 (1994) 184 and references therein.

[26] F.M. Renard, Phys. Lett. B116 (1982) 264; J. Kühn and P. Zerwas, Phys. Lett. B147 (1984) 189.

[27] CHARM Collaboration, J. Dorenbosch *et al.*,

[28] UA2 Collaboration, J. Alitti *et al.*, Nucl. Phys. B400 (1993) 3.

[29] CDF Collaboration, F. Abe *et al.*, Phys. Rev. Lett. 72 (1994) 3004.
[30] H1 Collaboration, T. Ahmed *et al.*, DESY-94-138.
[31] S. J. Brodsky and S. D. Drell, Phys. Rev. D22 (1980) 2236.

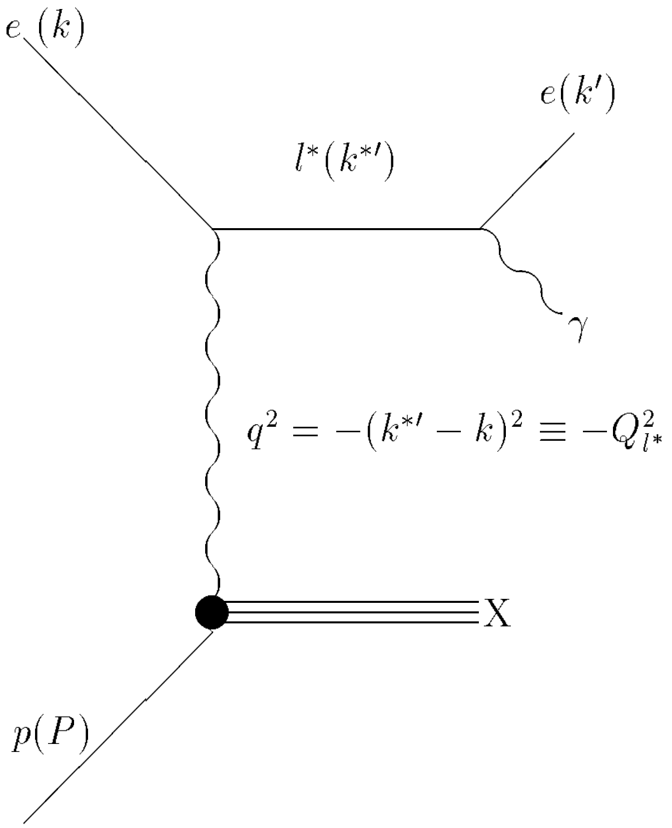

FIG. 1. Feynman diagram of excited lepton production in ep collisions. Shown is the decay of the excited electron into an electron and a photon. Other possible decays include $e^* \to eZ$ and $e^* \to \nu W$.

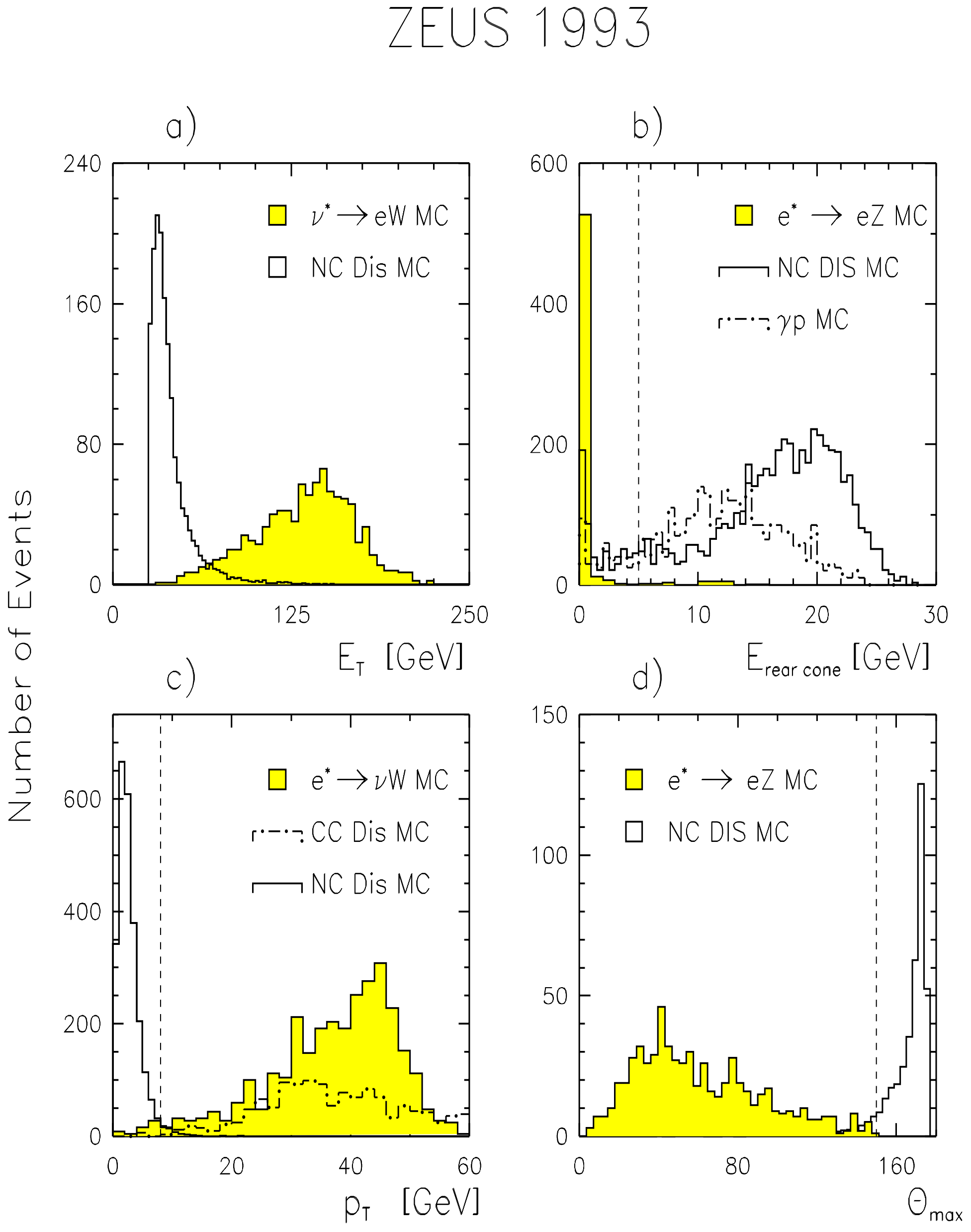

FIG. 2. Fiducial data sample distributions for: a) transverse energy, E_T (after an $E_T > 20$ GeV cut); b) energy in backward cone; c) transverse momentum, p_T; d) largest polar angle (in degrees) of all electromagnetic clusters in the event.

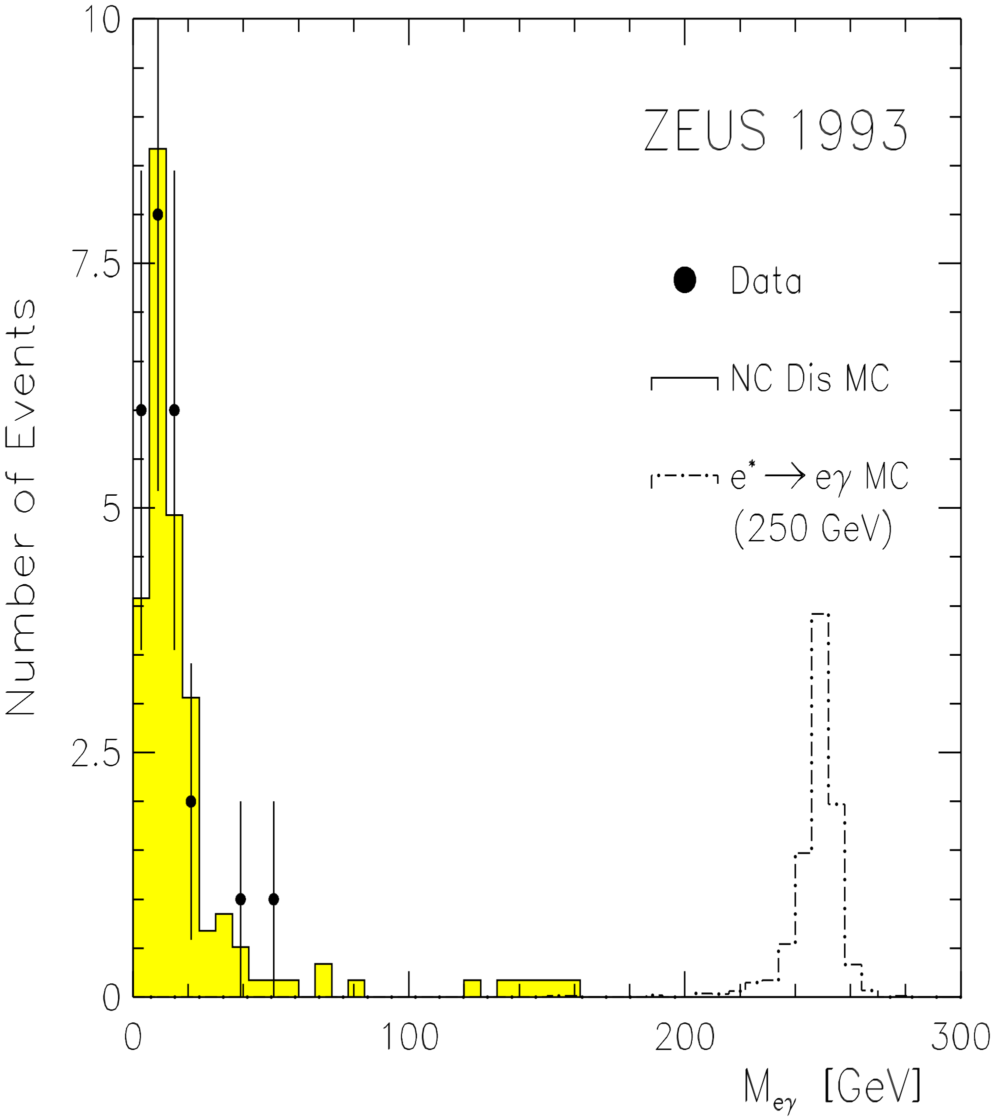

FIG. 3. Invariant $e\gamma$ mass for $e^* \rightarrow e\gamma$ candidates. The overlaid distribution from NC DIS Monte Carlo predictions (shaded histogram) is normalized to the data luminosity. Also shown is the signal expected for a 250 GeV excited electron (dash-dotted histogram) decaying to a photon and an electron (arbitrary normalization).

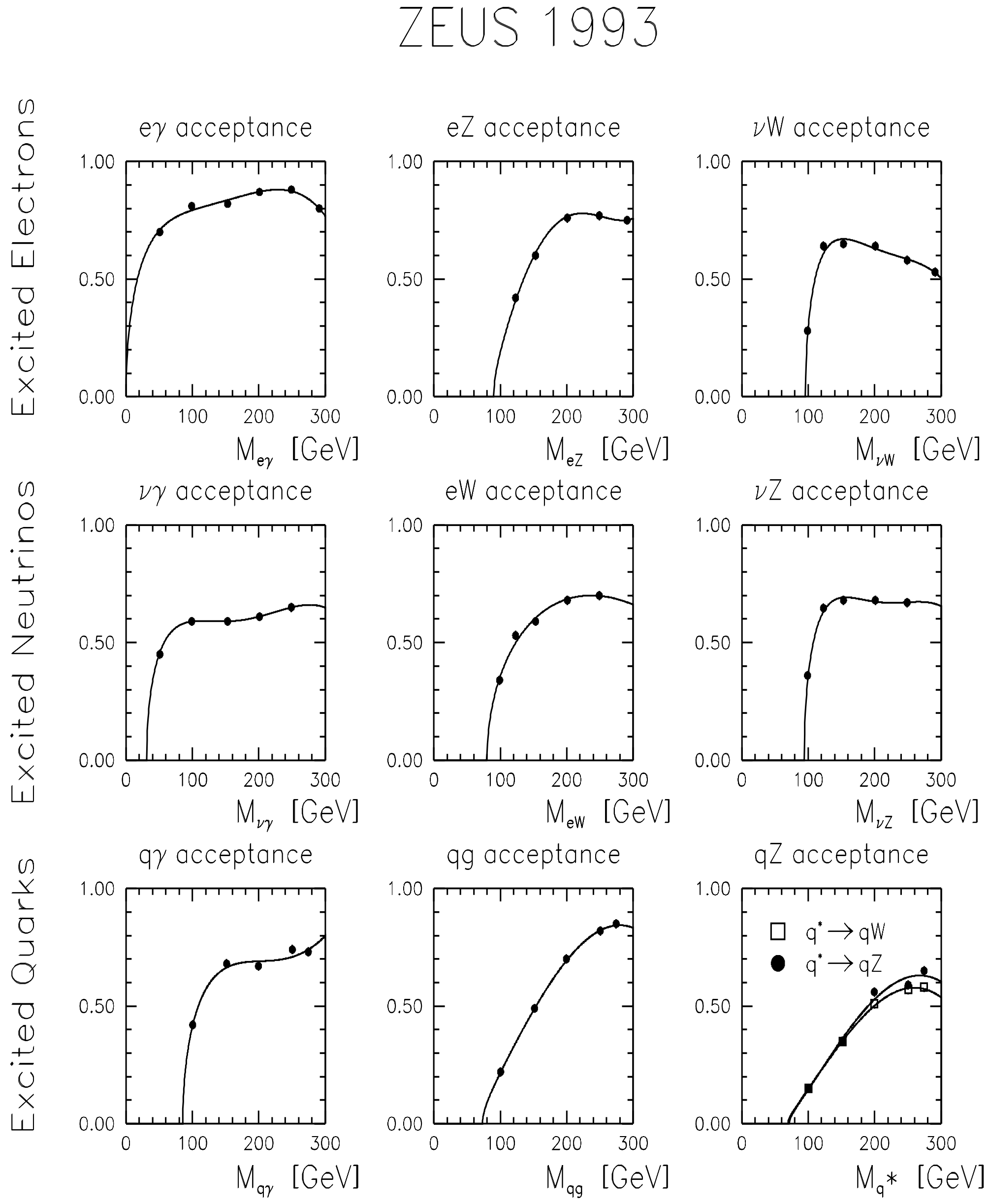

FIG. 4. Overall efficiency (after ZEUS detector simulation and analysis cuts) for excited electrons (1st row), excited neutrinos (2nd row), and excited quarks (3rd row) as a function of the generated mass of the excited fermion.

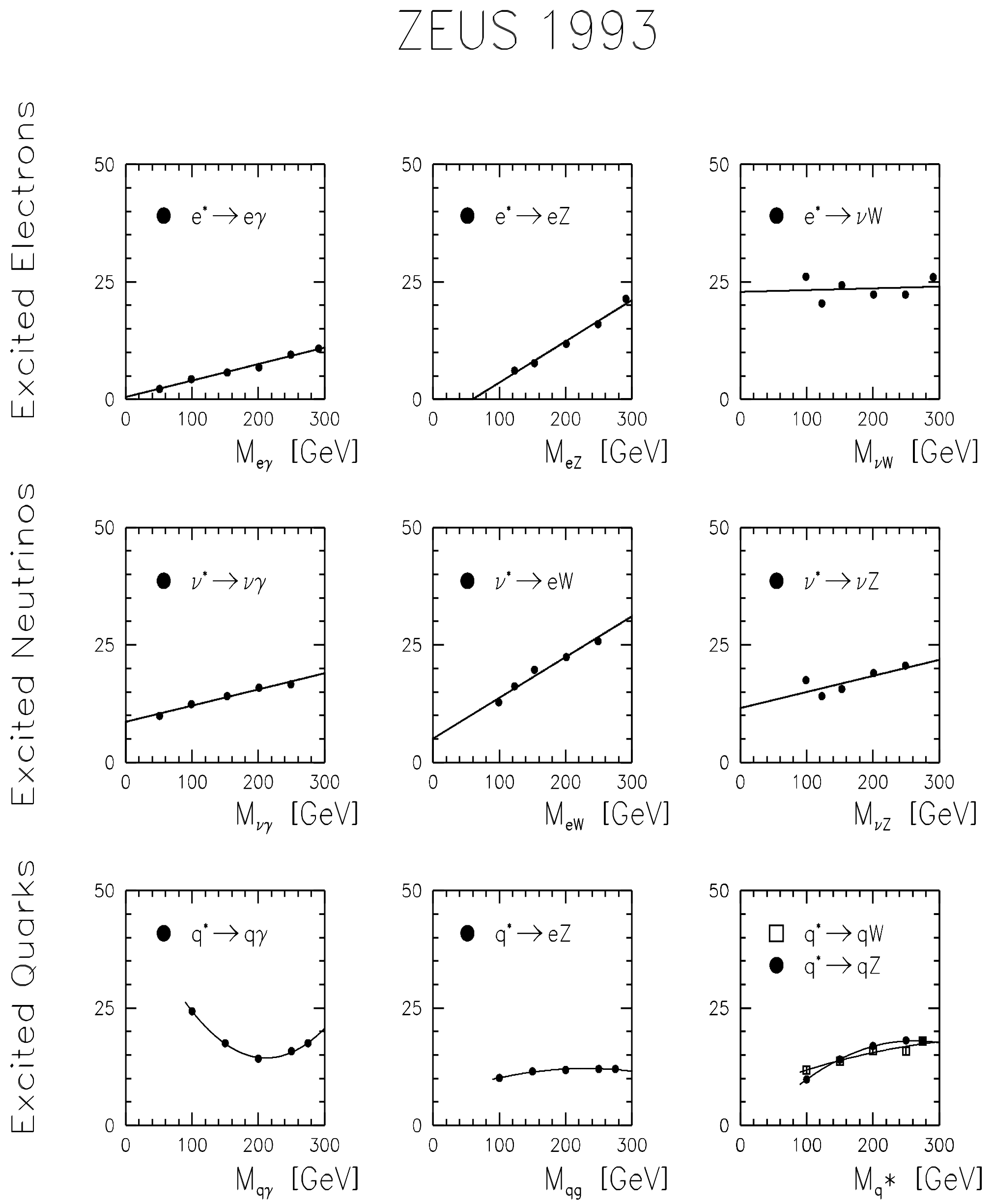

FIG. 5. Width of reconstructed mass-peak (in GeV) for excited electrons (1st row), excited neutrinos (2nd row), and excited quarks (3rd row) as a function of the generated mass of the excited fermion.

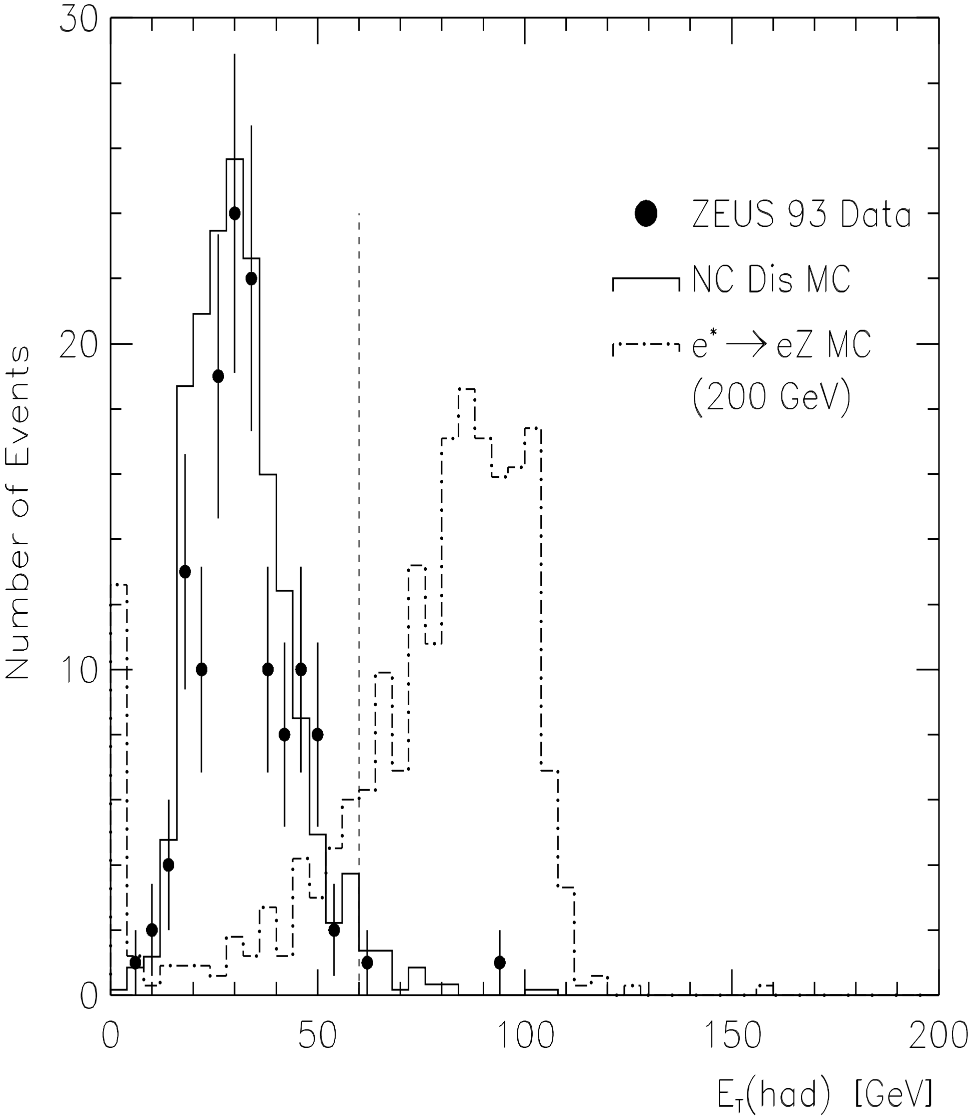

FIG. 6. Hadronic transverse energy distributions for data with the normalized Monte Carlo NC DIS background (solid histogram) overlaid. The position of the analysis cut is indicated by the dashed line. Also shown is the hadronic transverse energy distribution for a 200 GeV excited electron (dash-dotted histogram) decaying to an eZ final state (arbitrary normalization).

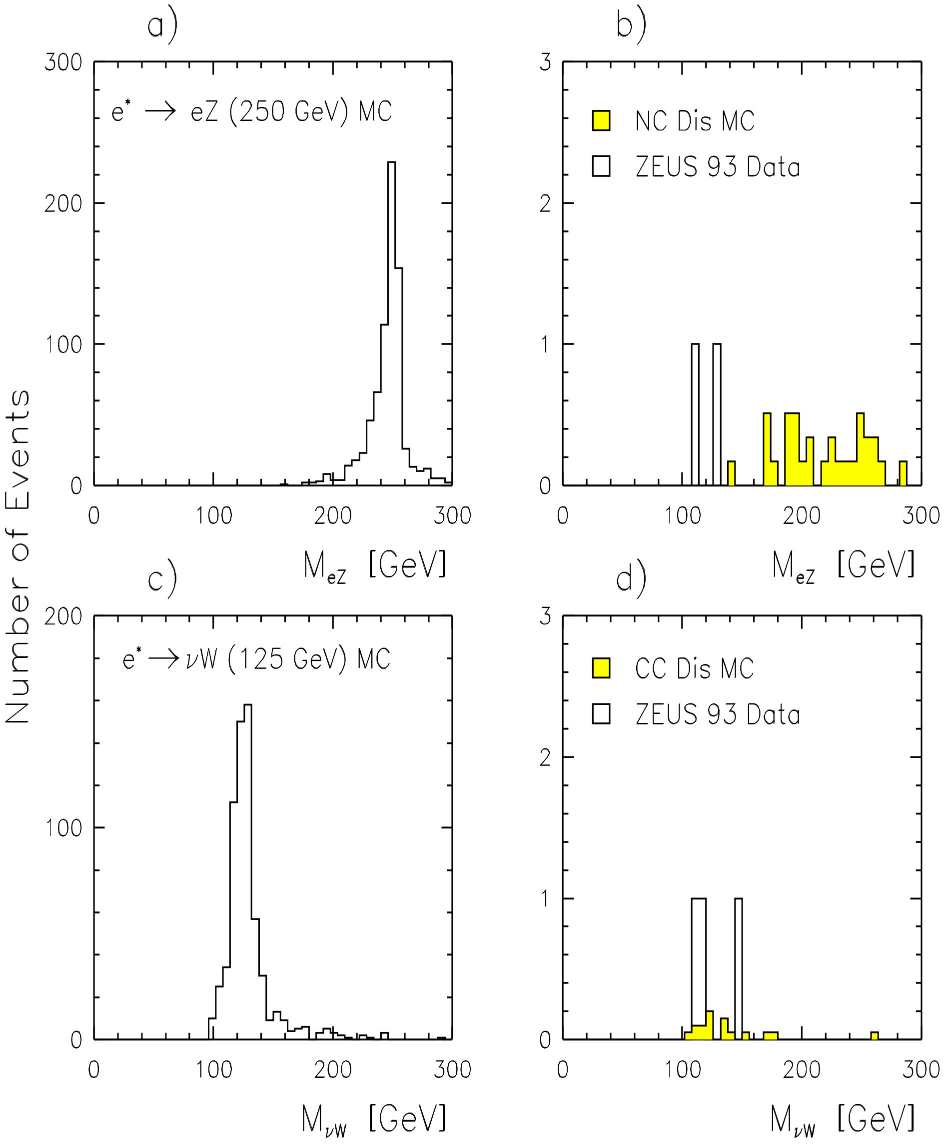

FIG. 7. Invariant eZ mass distributions: a) 250 GeV excited electron decaying to eZ; b) data with the normalized Monte Carlo NC DIS background (shaded histogram) overlaid. Invariant νW mass distributions: c) 125 GeV excited electron decaying to νW; d) data with the normalized Monte Carlo CC DIS background (shaded histogram) overlaid.

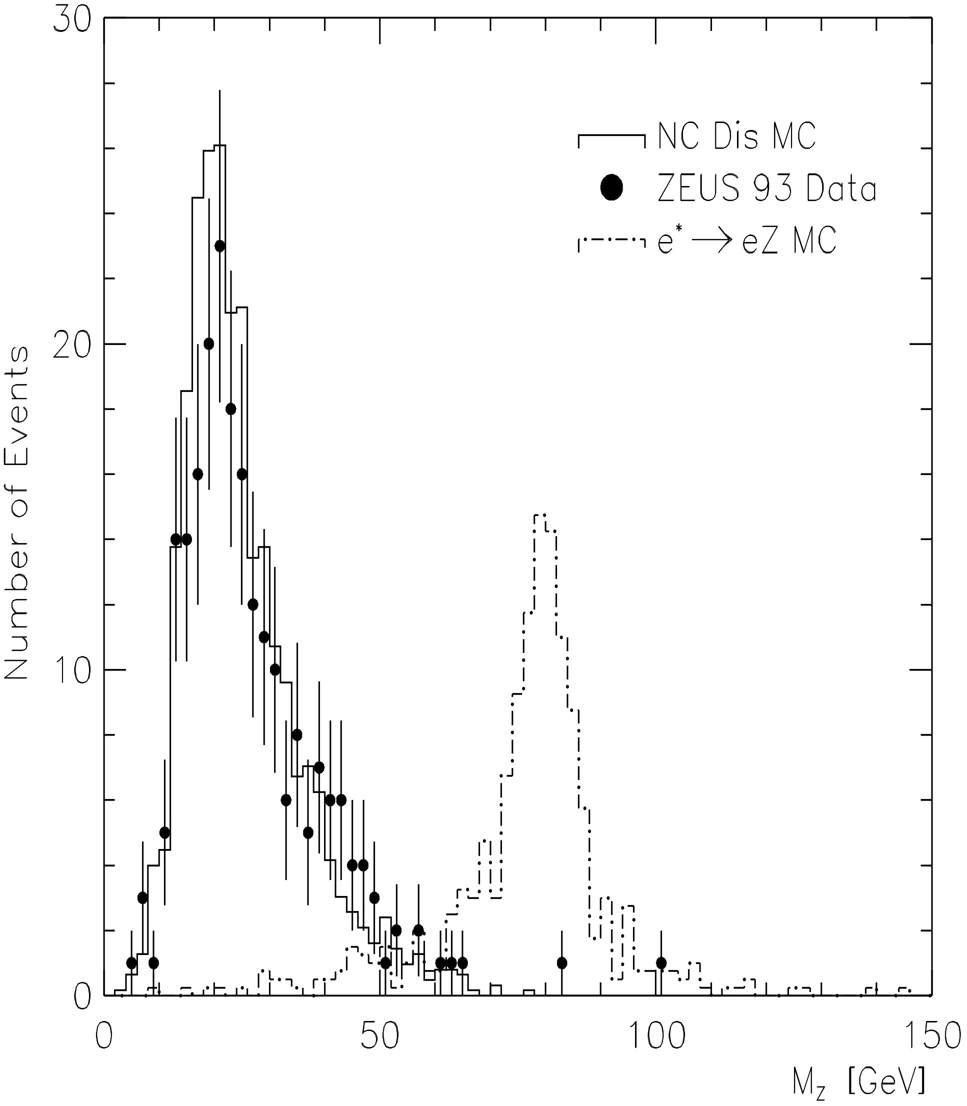

FIG. 8. Invariant mass calculated from the calorimeter energy deposits but excluding the tagged electron cluster and the cells from the FCAL inner ring for data and normalized NC DIS Monte Carlo background. Also shown is the reconstructed Z mass (dash-dotted histogram) from $e^* \to eZ$ (125 GeV) Monte Carlo.

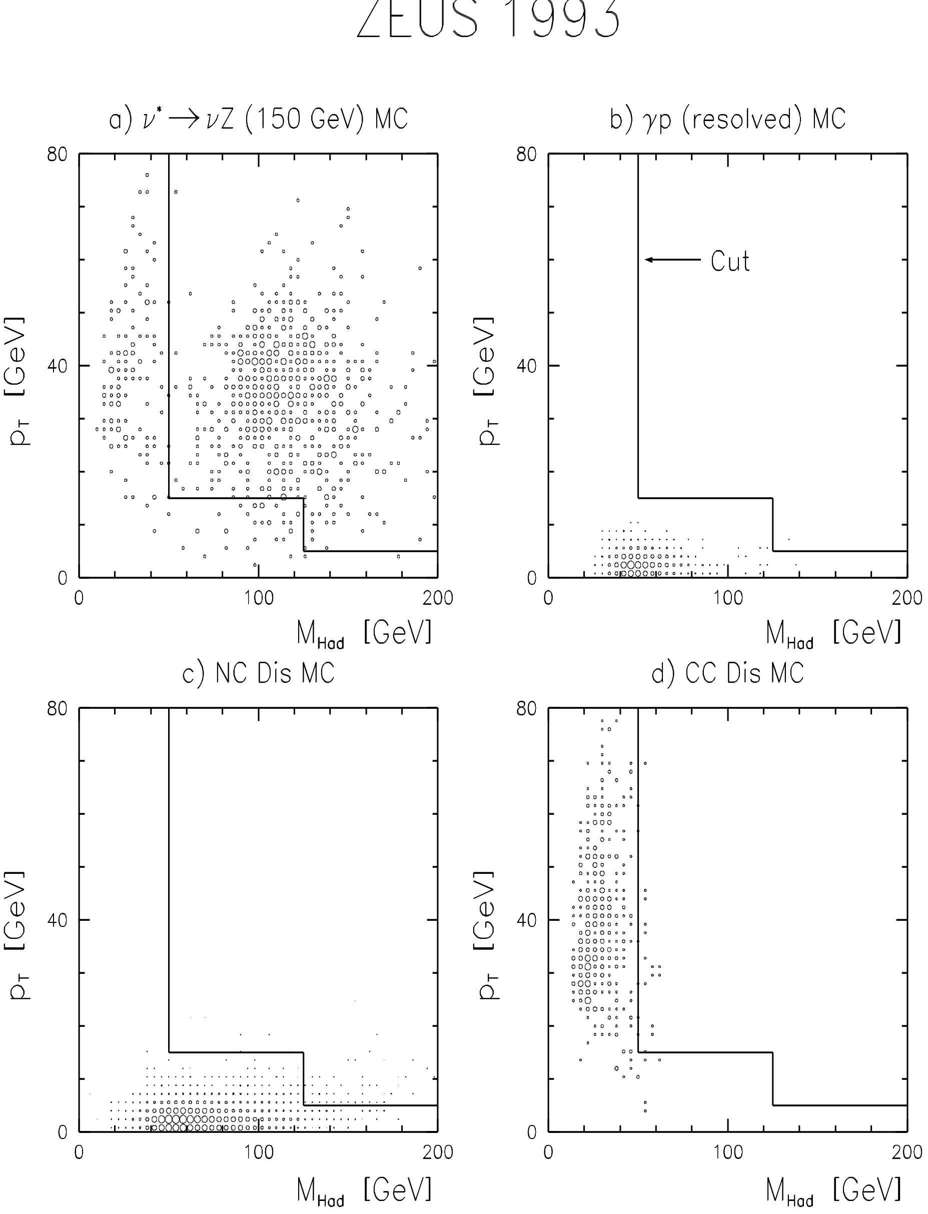

FIG. 9. Distribution of hadronic invariant mass (excluding the inner FCAL ring) versus transverse momentum for $\nu^* \rightarrow \nu Z$ events: a) for 150 GeV ν^*s decaying to νZ for a Monte Carlo (MC) simulation; b) background from resolved photoproduction MC; c) background from neutral current DIS MC; d) background from charged current DIS MC.

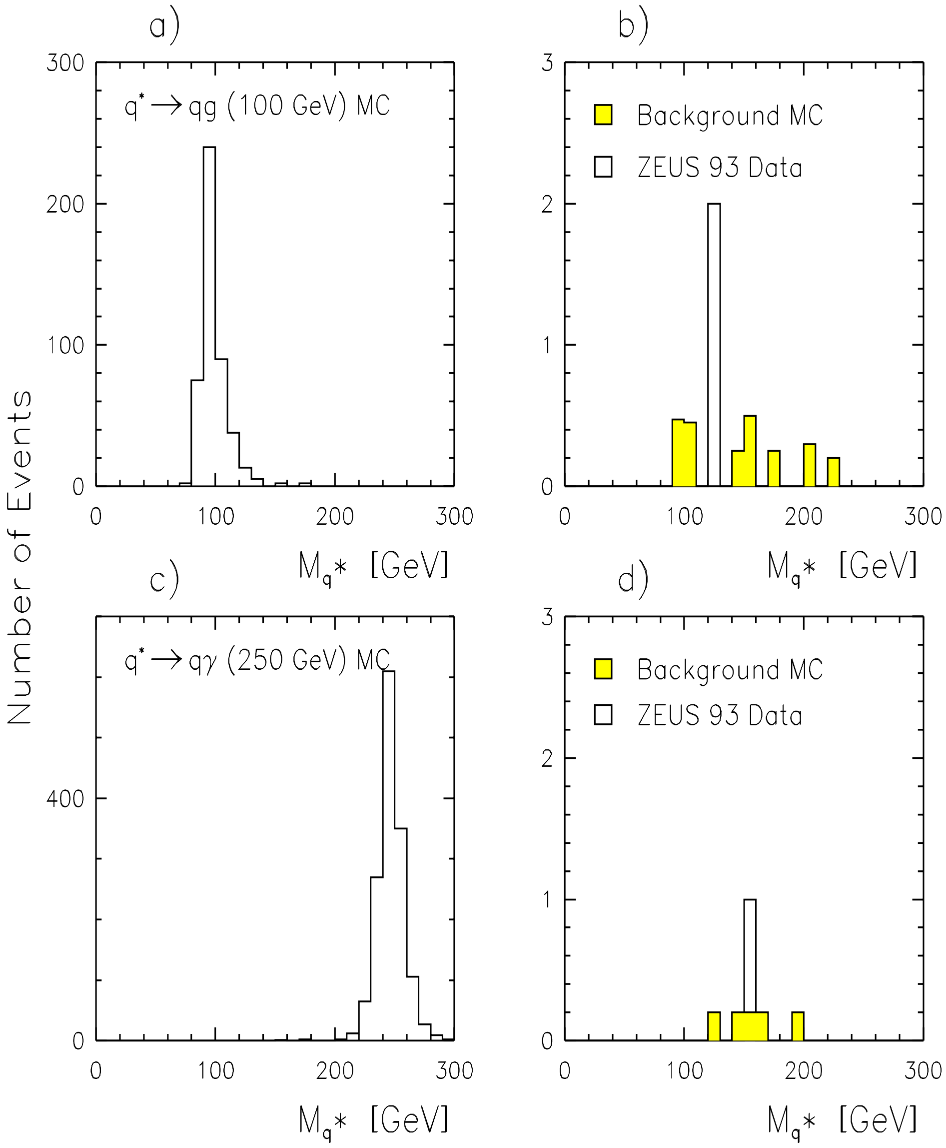

FIG. 10. Invariant qg (qW, qZ) mass distributions: a) 100 GeV excited quark decaying to qg; b) ZEUS 1993 data with the normalized Monte Carlo background overlaid. Invariant $q\gamma$ mass distributions: c) 250 GeV excited quark decaying to $q\gamma$; d) ZEUS 1993 data with the normalized Monte Carlo background overlaid.

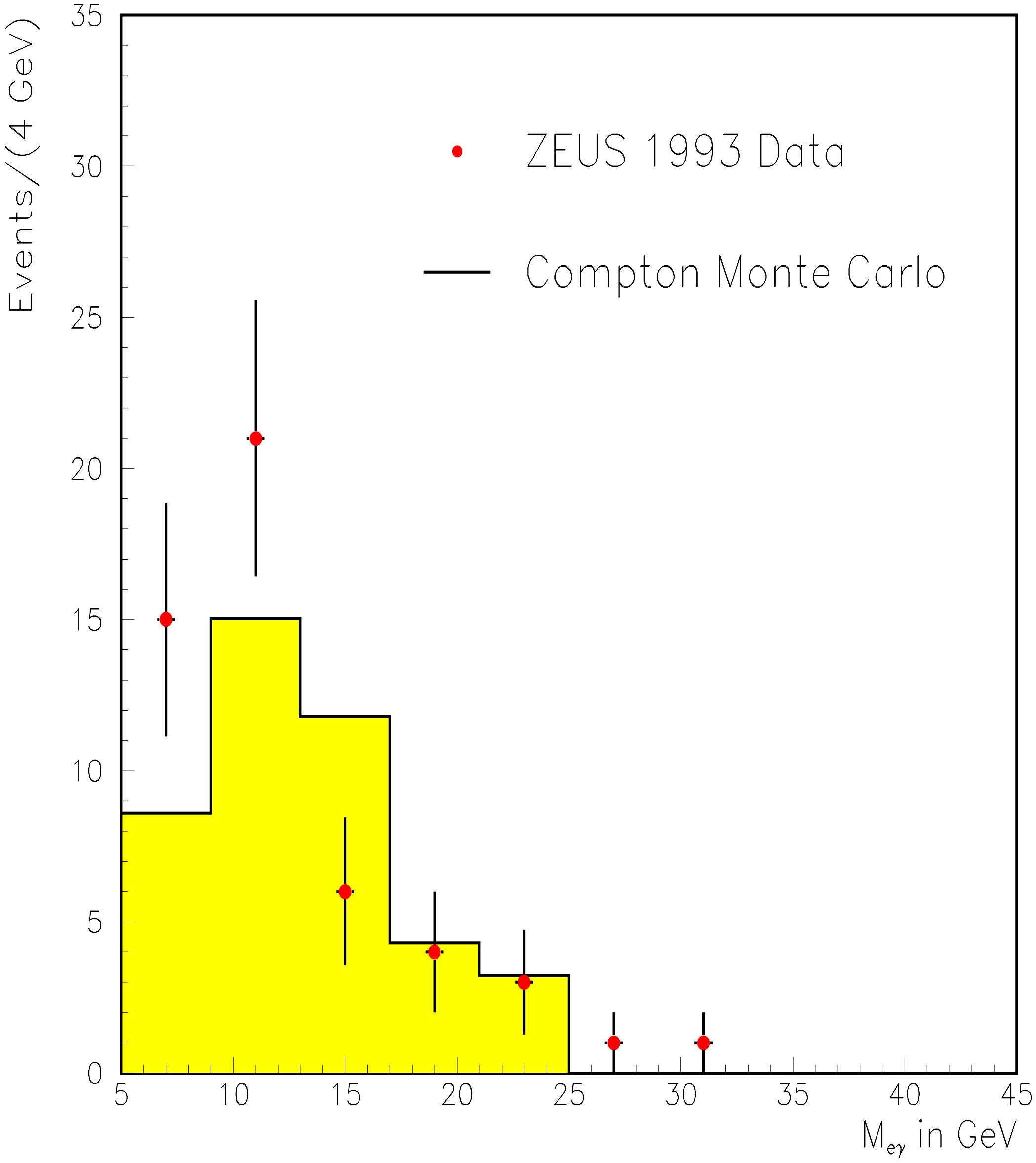

FIG. 11. Distribution of the $e\gamma$ invariant mass for events in the Compton data sample. Shown are the events in data (points with error bars) and normalized Compton Monte Carlo predictions (shaded histogram).

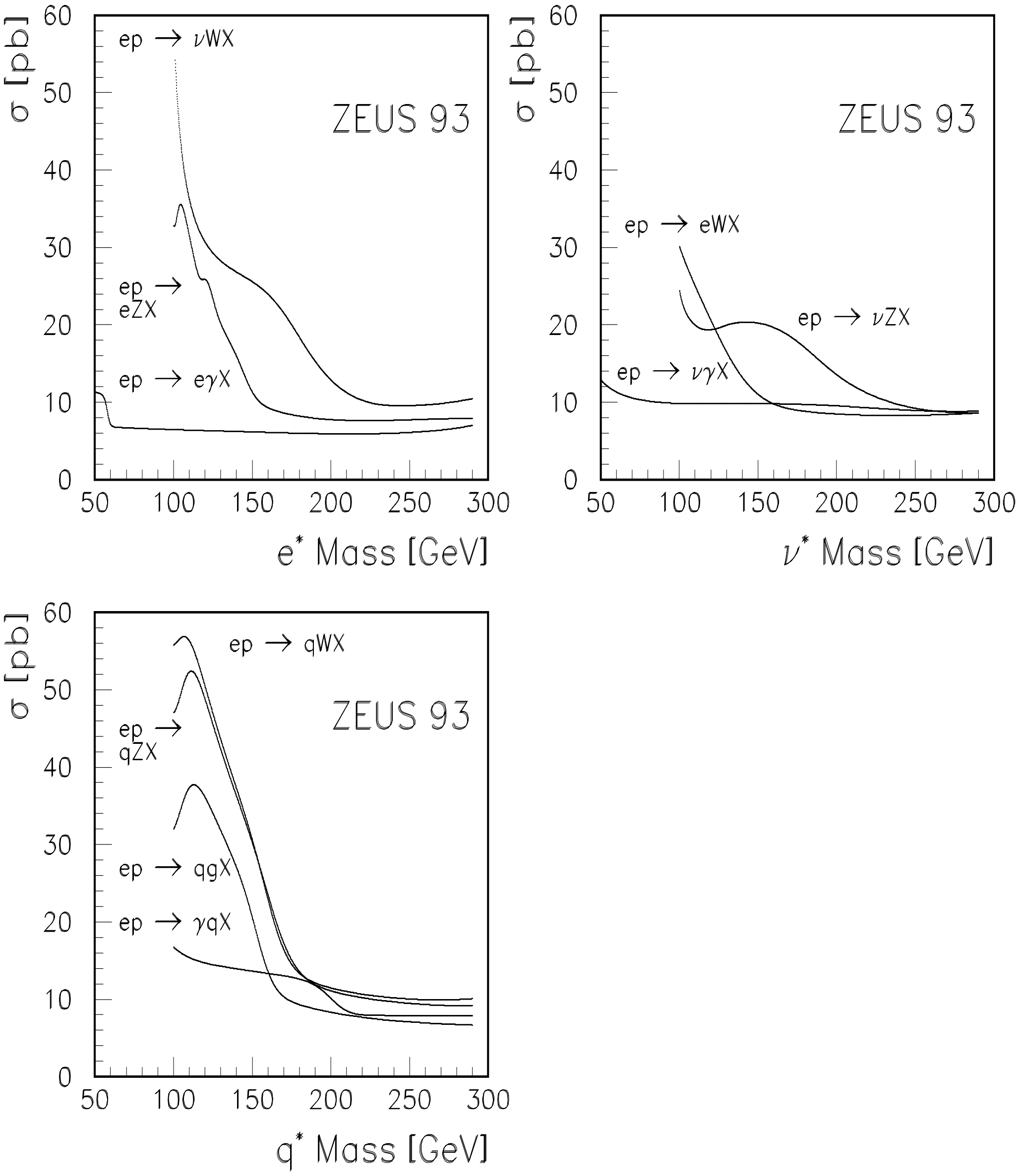

FIG. 12. 95% confidence level upper limits on production cross-sections for a heavy resonance decaying to fermion – gauge boson final states: a) final states accessible to an excited electron; b) final states accessible to an excited neutrino; c) final states accessible to an excited quark. The dip near 100 GeV seen in some channels results from the proximity of a candidate event.

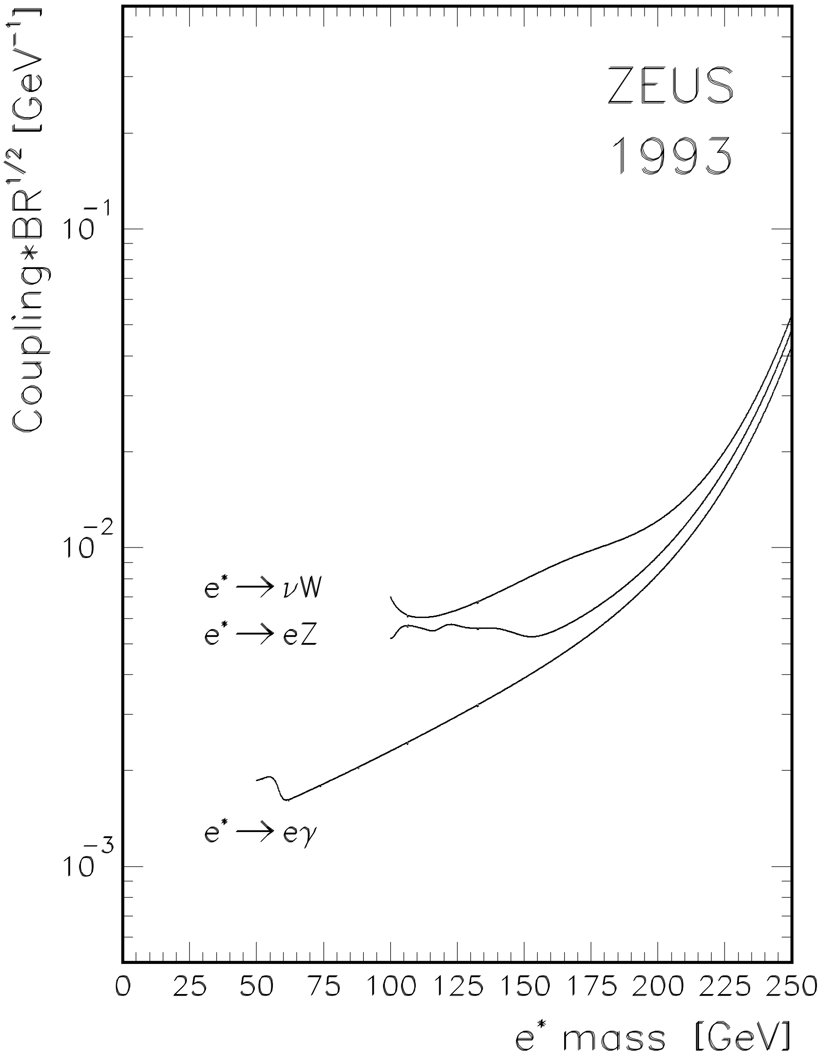

FIG. 13. 95% confidence level upper limits on the product of the coupling constant, $\sqrt{|c_{\gamma e^* e}|^2 + |d_{\gamma e^* e}|^2)}/\Lambda$, and the square root of the branching ratio (BR), for excited electrons decaying to $e\gamma$, eZ, and νW final states. In each channel the area above the curve is excluded. Note that these limits must be divided by $\sqrt{2}$ when comparing with some published limits [5] [6] [30].

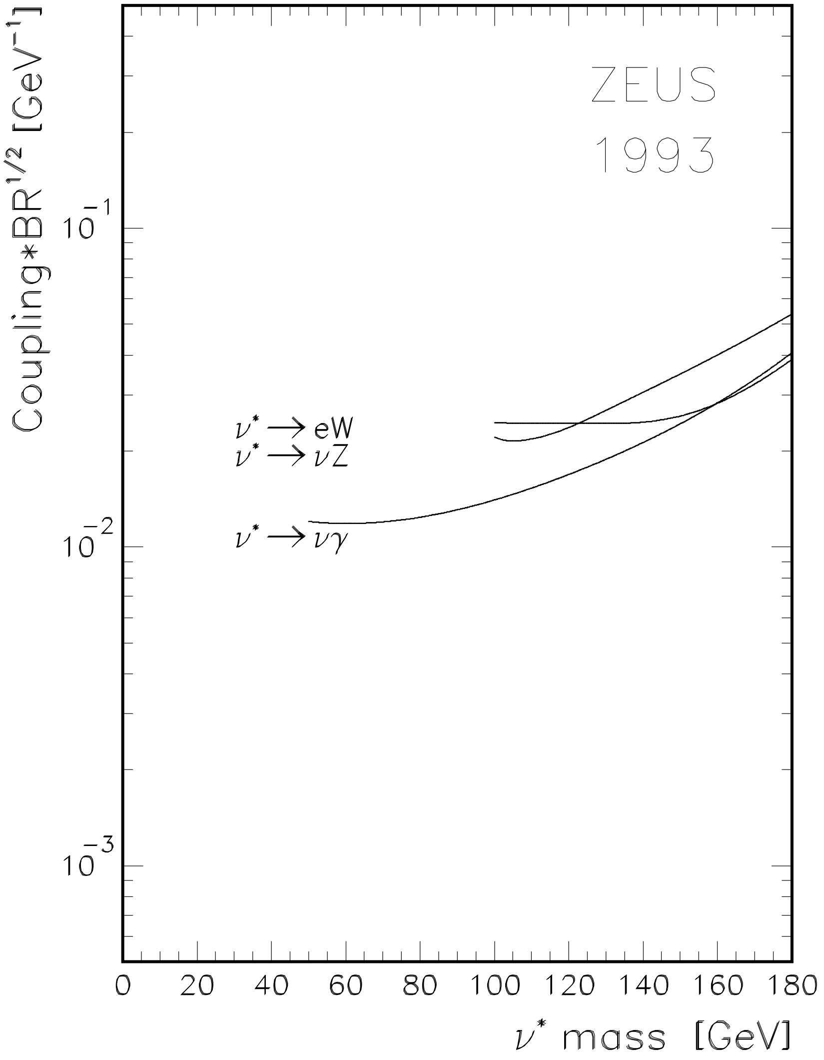

FIG. 14. 95% confidence level upper limits on the product of the coupling constant, $\sqrt{(|c_{W\nu^* e}|^2 + |d_{W\nu^* e}|^2)}/\Lambda$, and the square root of the branching ratio (BR), for excited neutrinos decaying to $\nu\gamma$, νZ, and eW final states. In each channel the area above the curve is excluded. Note that these limits must be divided by $\sqrt{2}$ when comparing with some published limits [5] [6] [30].

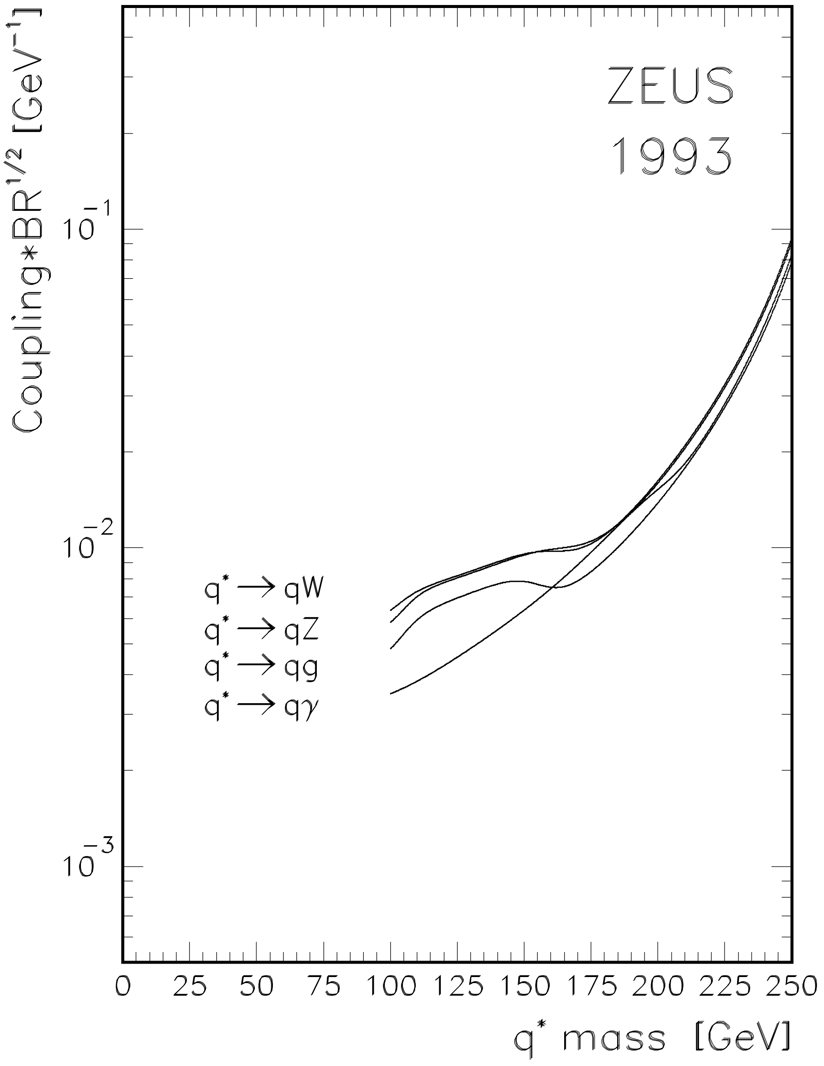

FIG. 15. 95% confidence level upper limits on the product of the coupling constant, $\sqrt{(|c_{\gamma q^* q}|^2 + |d_{\gamma q^* q}|^2)}/\Lambda$, and the square root of the branching ratio (BR), for excited quarks decaying to $q\gamma$, qZ, qW, and qg final states. In each channel the area above the curve is excluded. Note that these are limits on q^* production through electroweak coupling.